

The High-Mass End of the Black Hole Mass Function: Mass Estimates in Brightest Cluster Galaxies¹

E. Dalla Bontà

Dipartimento di Astronomia, Università degli Studi di Padova, Padova, Italy

Herzberg Institute of Astrophysics, Victoria, CA

`elena.dallabonta@unipd.it`

L. Ferrarese

Herzberg Institute of Astrophysics, Victoria, CA

`laura.ferrarese@nrc-cnrc.gc.ca`

E. M. Corsini

Dipartimento di Astronomia, Università degli Studi di Padova, Padova, Italy

`enricomaria.corsini@unipd.it`

J. Miralda-Escudé

Institut de Ciències de l'Espai (IEEC-CSIC/ICREA)

`miralda@aliga.ieec.uab.es`

L. Coccato

Max-Planck-Institut fuer extraterrestrische Physik, Garching bei Muenchen, Germany

`lcoccatompe.mpg.de`

M. Sarzi

Centre for Astrophysics Research, University of Hertfordshire, Hatfield, UK

`m.sarzi@herts.ac.uk`

A. Pizzella

Dipartimento di Astronomia, Università degli Studi di Padova, Padova, Italy

`alessandro.pizzella@unipd.it`

and

A. Beifiori

Dipartimento di Astronomia, Università degli Studi di Padova, Padova, Italy

alessandra.beifiori@unipd.it

ABSTRACT

We present Hubble Space Telescope imaging and spectroscopic observations of three Brightest Cluster Galaxies, Abell 1836-BCG, Abell 2052-BCG, and Abell 3565-BCG, obtained with the Wide Field and Planetary Camera 2, the Advanced Camera for Surveys and the Space Telescope Imaging Spectrograph. The data provide detailed information on the structure and mass profile of the stellar component, the dust optical depth, and the spatial distribution and kinematics of the ionized gas within the innermost region of each galaxy. Dynamical models, which account for the observed stellar mass profile and include the contribution of a central supermassive black hole (SBH), are constructed to reproduce the kinematics derived from the $H\alpha$ and $[N\ II]\lambda\lambda 6548, 6583$ emission lines. Secure SBH detection with $M_{\bullet} = 3.61_{-0.50}^{+0.41} \times 10^9 M_{\odot}$ and $M_{\bullet} = 1.34_{-0.19}^{+0.21} \times 10^9 M_{\odot}$, respectively, are obtained for Abell 1836-BCG and Abell 3565-BCG, which show regular rotation curves and strong central velocity gradients. In the case of Abell 2052-BCG, the lack of an orderly rotational motion prevents a secure determination, although an upper limit of $M_{\bullet} \lesssim 4.60 \times 10^9 M_{\odot}$ can be placed on the mass of the central SBH. These measurements represent an important step forward in the characterization of the high-mass end of the SBH mass function.

Subject headings: black hole physics — galaxies: elliptical and lenticular, cD — galaxies: nuclei — galaxies: kinematics and dynamics

1. Introduction

Within the past decade, the focus in supermassive black holes (SBHs) studies has moved from the dynamical measurement of SBH masses, M_{\bullet} , in nearby galaxies (see review by Ferrarese & Ford 2005), to the characterization of scaling relations connecting M_{\bullet} to the large

¹Based on observations made with ESO telescopes at the La Silla Paranal Observatory under programme ID 279.B-5004(A).

scale properties of their hosts (Kormendy & Richstone 1995; Ferrarese & Merritt 2000; Gebhardt et al. 2000; Graham et al. 2001; Ferrarese 2002; Marconi & Hunt 2003). Such relations, combined with the knowledge of the galaxy luminosity or velocity dispersion functions, lead to a direct determination of the local SBH mass function and, by comparison with the energetics of high redshift AGNs, accretion history (e.g. Marconi et al. 2004; Shankar et al. 2004; Benson et al. 2007; Tundo et al. 2007; Graham et al. 2007; Lauer et al. 2007). Furthermore, the tightness of the relations linking galactic properties to M_{\bullet} is indicative of a formation/evolutionary history in which SBHs and galaxies are causally connected. Indeed, feedback from AGN activity is believed to play an important, perhaps even fundamental role in the evolution of galaxies (e.g. Binney & Tabor 1995; Suchkov et al. 1996; Ciotti & Ostriker 2001; Schawinski et al. 2006; Springel et al. 2005; Hopkins et al. 2007; Di Matteo et al. 2007).

In this context, Brightest Cluster Galaxies (BCGs) are of particular interest. Their privileged location at the center of a massive cluster implies that they have undergone a particularly extensive merging history (Khochfar & Silk 2006) and are likely to host the most massive SBHs in the local Universe (Yoo et al. 2007). The latter conclusion is also supported by all scaling relations which are known to be obeyed by local SBHs, that predict the most massive SBHs to reside in most massive galaxies. As such, BCGs constitute an excellent laboratory to search for the local relics of the most powerful high-redshift quasars (Willott et al. 2003; Vestergaard 2004), and to investigate the role of mergers in the black hole mass function.

Unfortunately, direct dynamical measurements of SBHs masses in BCGs are exceedingly difficult - with only two such measurements made to-date (in M87 and NGC 1399, Harms et al. 1994; Macchetto et al. 1997; Houghton et al. 2006). The reason for this is simple: SBH mass measurements based on resolved kinematic tracers (gas or stars) need to be carried out within the SBH “sphere of influence”, i.e. the region of space within which the SBH dominates the overall gravitational potential. For a $10^9 M_{\odot}$ SBH, the sphere of influence becomes unresolved for optical measurements with the Hubble Space Telescope at distances beyond ~ 100 Mpc (see Figure 44 of Ferrarese & Ford 2005). Few BCGs are located within this limit. To compound the problem, bright ellipticals are characterized by shallow stellar density profiles and faint central surface brightnesses (e.g., Ferrarese et al. 1994; Lauer et al. 1995; Rest et al. 2001; Ferrarese et al. 2006) making the detection of stellar absorption lines with *HST* prohibitively expensive. The latter difficulty can be overcome with the use of gas dynamics. Emission lines (mainly $H\alpha$ and [N II]) from the gas are bright and easily measured. If the gas is confined in a disk, there is little ambiguity in the velocity distribution (Ho et al. 2002), and since the method was first used (Harms et al. 1994; Ferrarese et al. 1996; Ferrarese & Ford 1999) an increasing amount of attention has been devoted to the

theoretical aspects of the dynamical modeling (Maciejewski & Binney 2001; Barth et al. 2001; Cappellari et al. 2002; Coccato et al. 2006).

The lack of a secure characterization of the SBH mass function above the $10^9 M_\odot$ mark is troublesome. Lauer et al. (2007) suggest that the relations between M_\bullet and host bulge luminosity, L_{bulge} , (Kormendy & Richstone 1995) and velocity dispersion (Ferrarese & Merritt 2000; Gebhardt et al. 2000) would predict significantly different M_\bullet if extrapolated above $10^9 M_\odot$. In particular, the $M_\bullet - \sigma$ relation would predict less massive SBHs in BCGs than the $M_\bullet - L_{bulge}$ relation, due to the slower increase of σ with galaxy luminosity observed for BCGs compared to the bulk of the Early-Type galaxy population (Bernardi et al. 2007). The difference in the predicted mass is such to significantly affect (by an order of magnitude) the high-mass end of the local SBH mass function. von der Linden et al. (2007) argue that the shallower dependence of σ on L applies to BCG but not to comparably massive non-BCG galaxies, which instead follow the canonical Faber-Jackson relation defined by less massive systems. This implies that BCGs and non-BCG galaxies of comparable mass must occupy a different locus in either, or both, the $M_\bullet - \sigma$ and $M_\bullet - L_{bulge}$. This result is in contrast with the findings of Batcheldor et al. (2007), who argue that SBHs masses predicted from NIR luminosities (Marconi & Hunt 2003) are consistent with those predicted from σ . They attributed the discrepancy noted by Lauer et al. (2007) (who used V -band luminosities) to a bias introduced by the inclusion, when computing L_{bulge} , of extended blue envelopes around BCGs. At present these ambiguities prevent us from testing any theoretical prediction on the high-mass end of the black hole mass function based on the observed quasar abundances and merger histories.

In this paper, we analyze the kinematics of the ionized gas in the nuclear region of three BCGs – Abell 1836-BCG, Abell 2052-BCG, and Abell 3565-BCG – in order to constrain the mass of the central SBHs. The data were obtained using the Space Telescope Imaging Spectrograph (STIS) on board the Hubble Space Telescope (HST), supplemented with imaging data from the Advanced Camera for Surveys (ACS) and the Wide Field and Planetary Camera 2 (WFPC2). Furthermore, the central stellar velocity dispersion of Abell 1836-BCG was obtained from ground based spectroscopy. The paper is organized as follows. The criteria of galaxy selection are presented in §2. ACS and STIS observations are described and analyzed in §§3 and 4, respectively. Ground based spectroscopic observations of Abell 1836-BCG are described and analyzed in §5.

The SBH masses of Abell 1836-BCG and Abell 3565-BCG, and an upper limit for the SBH mass of Abell 2052-BCG are derived in §6. In §7 results are compared to the predictions of the SBHs scaling laws and conclusions are given.

2. Galaxy sample

Naturally, the place to search for the most massive black holes in the universe is in the most nearby and most massive BCGs, where the problems of angular resolution to measure black hole masses are minimized. The galaxies discussed in this contribution were selected from the BCG sample observed by Laine et al. (2003) with the HST Wide Field and Planetary Camera 2 (WFPC2). Dynamical studies in giant ellipticals are performed more effectively by modeling gas, rather than stellar kinematics (see discussion in Ferrarese & Ford 2005), both because of the low stellar surface brightness that characterizes the core regions of such systems (e.g. Ferrarese et al. 2006) and because when applied to slowly-rotating, pressure supported galaxies, stellar dynamical models depend heavily on the knowledge of the anisotropy in the stellar velocity dispersion, a difficult quantity to constrain observationally (e.g. van der Marel 1998). Eleven of the 81 galaxies in the Laine et al. (2003) sample appear to contain well defined nuclear dust structures, which can trace regular gas kinematics (Ho et al. 2002). After selecting the most regular nuclear dust structures among those eleven objects and after excluding galaxies for which existing ground based spectra showed no evidence of nuclear $H\alpha$ and $[N II] \lambda\lambda 6548, 6583$ in emission, we selected the four BCGs predicted to host the most massive SBHs (based on the correlations between black hole mass, M_\bullet , and the host bulge stellar velocity dispersion, σ , and/or B -band luminosity, L_B) and for which the SBH sphere of influence could be well resolved using the $0''.1$ wide slit of HST’s Space Telescope Imaging Spectrograph (STIS).

One galaxy (Abell 2593-BCG) was not observed due to the premature failure of STIS. The sample discussed in this paper therefore includes three BCGs, namely Abell 1836-BCG (PGC 49940), Abell 2052-BCG (UGC 9799) and Abell 3565-BCG (IC 4296). The main properties of these galaxies are summarized in Table 1.

3. Observations, data reduction, and analysis: Imaging

3.1. Observations and data reduction

The luminosity density and ionized gas distribution of the target galaxies, both of which are required for the dynamical modeling described in §6, have been constrained using HST ACS and WFPC2 images. Basic information about the data can be found in Table 2.

The ACS images were obtained with the High Resolution Channel (HRC) as part of program GO-9838 (P.I. L. Ferrarese). The HRC detector is a 1024×1024 SITe CCD with a plate scale of $0''.028 \times 0''.025 \text{ pixel}^{-1}$. Because of the large, but well characterized, geometric

distortion affecting the ACS, the $29'' \times 26''$ HRC field of view projects on the plane of the sky as a rhomboid with x and y axes forming a $84^\circ 2'$ angle. Each galaxy was observed with two filters: F435W (which approximates the Johnson B -band) and the narrow-band ramp filter FR656N, tuned to cover a 130 \AA wide spectral region centered on the redshifted $H\alpha$ and $[\text{N II}] \lambda\lambda 6548, 6583$ emission expected at the nuclear location. To help in identifying and correcting cosmic ray events, two back-to-back exposures were taken with each filter.

The WFPC2 images, all employing the F814W filter (similar to the Kron-Cousin I band), belong to programs GO-5910 (P.I. T. Lauer) and GO-8683 (P.I. R.P. van der Marel) and were downloaded from the public HST archive. Two images with a total exposure time of 1000 s are available for each Abell 1836-BCG and Abell 2052-BCG, while ten images are available for Abell 3565-BCG, for a total 11,600 s exposure. In all cases, the galaxies are centered on the higher resolution Planetary Camera (PC), which consists of an 800×800 pixels Loral CCD with a plate scale of $0''.0455 \text{ pixel}^{-1}$, yielding a nominal field of view of $36'' \times 36''$. For both ACS and WFPC2 images, the telescope was guiding in fine lock, giving a typical rms tracking error per exposure of $0''.005$.

All images were calibrated using the standard reduction pipelines maintained by the Space Telescope Science Institute (PyRAF/CalACS for the ACS images and IRAF/CalWFPC for the WFPC2 images). Reduction steps include bias subtraction, dark current subtraction and flat-fielding, as described in detail in the ACS and WFPC2 instrument and data handbooks (Baggett et al. 2002; Heyer et al. 2004; Pavlovsky et al. 2004a,b).

Subsequent analysis was performed using standard tasks in IRAF². For each galaxy, the alignment of images obtained with the same instrument and filter was checked by comparing the centroids of stars in the field of view; in all cases but one, the alignment was found to be better than a few hundredths of a pixel and the images were combined without further processing using IRAF/IMCOMBINE. The exception are the WFPC2 images of Abell 3565-BCG, which were dithered by $\approx 1''$ relative to one another. These images were aligned using IMSHIFT prior to being combined.

In combining the images, pixels deviating by more than three times the local sigma – calculated from the combined effect of Poisson and read-out noise – were flagged as cosmic rays and rejected. Finally, the resulting ACS images were corrected for geometric distortion using PYRAF/PYDRIZZLE.

²IRAF is distributed by the National Optical Astronomy Observatories which are operated by the Association of Universities for Research in Astronomy (AURA) under cooperative agreement with the National Science Foundation.

The final, calibrated ACS and WFPC2 images of each galaxy are shown in Figures 1-3 and 4, respectively.

3.2. Isophotal analysis

Isophotal parameters (coordinates X, Y of the isophotal center; surface brightness profile $I(\phi)$; ellipticity ϵ ; major axis position angle θ ; and deviations of the isophotes from pure ellipses) were measured using the IRAF task ELLIPSE (Jedrzejewski 1987). For each semi-major axis length, the best fitting set of parameters X, Y, ϵ and θ are those that minimize the sum of the squares of the residuals between the data and the first two moments of the Fourier series expansion of the azimuthally-sampled intensity

$$I(\phi) = I_0 + \sum_k [A_k \sin(k\phi) + B_k \cos(k\phi)] \quad (1)$$

The third and fourth order moments (A_3, B_3, A_4 and B_4) describe three and four-fold deviations of the isophotes from pure ellipses, respectively. The B_4 term in particular describes the shape by distinguishing boxy ($B_4 < 0$) from diskly ($B_4 > 0$) galaxies.

The isophotal semi-major axis was increased logarithmically, with each isophote being fitted at a semi-major axis 10% longer than that of the isophote preceding it. The dust structure in Abell 2052-BCG is localized enough not to affect significantly the recovery of the underlying stellar distribution, so all parameters were allowed to vary freely while fitting the isophotes. For the other galaxies, a fully unconstrained isophotal solution could be found only in the regions unaffected by dust ($r > 0''.6$ and $r > 0''.9$ for Abell 1836-BCG and Abell 3565-BCG, respectively). In the areas affected by dust, the isophotes were fitted by fixing both ellipticity and position angle to the average values obtained in the dust-unaffected region ($0''.6 < r < 10''$ and $0''.9 < r < 10''$ for Abell 1836-BCG and Abell 3565-BCG, respectively). In all cases, pixels deviating by more than three times the standard deviation of the mean intensity along each trial isophote were excluded from the fit, thereby avoiding contamination by foreground stars, companion galaxies (as in the case of Abell 2052-BCG), globular clusters, and bad pixels. All isophotal parameters are plotted in Figures 5–7 as a function of the “geometric mean” radius r_{geo} , defined as $a[1 - \epsilon(a)]^{1/2}$, a being the semi-major axis length.

Conversion of $I(\phi)$ (which is given in counts per seconds) to surface brightness in the AB magnitudes system was performed following Holtzman et al. (1995) for the WFPC2 images, and Sirianni et al. (2005) for the ACS images:

$$\mu_{F814W} = -2.5 \log I_s(\phi)_{F814W} + 14.998, \quad (2)$$

$$\mu_{F435W} = -2.5 \log I_s(\phi)_{F435W} + 16.150, \quad (3)$$

where $I_s(\phi)_{F814W}$ and $I_s(\phi)_{F435W}$ represent the azimuthally averaged, background subtracted intensity (in counts per second per pixel) in F814W and F435W respectively. Because the galaxies completely fill the field of view of the ACS/HRC and WFPC2/PC detectors, a nominal sky background, as listed in the ACS (Pavlosky et al. 2004a) or WFPC2 (Heyer et al. 2004) Instrument Handbooks, was adopted.

3.3. Dust obscuration and optical depth map

Correction for dust obscuration is necessary to recover the intrinsic stellar luminosity density and the spatial distribution of the ionized gas within each galaxy. We adopted the procedure described in Ferrarese et al. (2006), which works under the assumption that the F435W-F814W intrinsic color of the galaxy in the regions obscured by dust can be estimated by linearly interpolating across the dust area (or extrapolating, if the dust affects the center) the azimuthally-averaged color measured in the regions unaffected by dust. The dust absorption at each pixel then follows by comparing the intrinsic and observed (extincted) color maps, once the ratio of the absorption in F435W and F814W is known (see equation 2 of Ferrarese et al. 2006). The latter, $A_{F435W}/A_{F814W} = 2.2814$ (where A_λ is given in magnitudes), has been derived using the extinction law of Cardelli et al. (1989), integrated over the filter passbands, and assuming a ratio of total-to-selective absorption $R_V = 3.1$ (see also Schlegel et al. 1998). It is further assumed that the dust lies in the galaxy foreground (the “screen” approximation); the values quoted below for the dust absorption therefore represent firm lower limits to the true absorption. Once the absorption in a specific passband is known, the intrinsic fluxes are easily recovered simply by correcting the measured fluxes for the derived magnitude loss due to dust obscuration.

In producing the F435W-F814W color maps, the ACS images were rotated (using the information about the position angle of the telescope axis contained in the header) and resampled using PYDRIZZLE in order to match the orientation and scale of the lower-resolution WFPC2 images.

Dust absorption maps are shown in the left panel of Figures 8–10. In Abell 1836-BCG, the average extinction (corrected to the V -band³) within the regular nuclear dust disk is $\langle A(V) \rangle = 0.27$ mag, with values as high as $A(V)_{max} = 0.85$ mag (in the screen approximation). The nuclear dust disk in Abell 3565-BCG is quite similar, with $A(V)_{max} =$

1.1 mag and $\langle A(V) \rangle = 0.21$ mag. Recovering a dust extinction map for Abell 2052-BCG, in which the dust is distributed in an irregular filamentary pattern and the amount of extinction is more modest, was more challenging. Within the inner $\approx 1''$, we find $A(V)_{max} = 0.35$ mag and $\langle A(V) \rangle = 0.14$ mag. At larger radii, dust patches with lower levels of dust obscuration, although visible in the color maps, could not be properly modeled. These areas, which affect less than 50% of pixels along any given isophote, were simply masked when deriving the galaxy’s surface brightness profile.

The extinction corrected F814W surface brightness profiles of the sample galaxies are shown in Figures 5–7.

3.4. Deprojected stellar density models

The deprojected luminosity density, $\Gamma(x, y, z)$, needed to constrain the stellar gravitational potential, was recovered from the redder (and thereby less affected by dust obscuration), extinction corrected, WFPC2/F814W images, using the multi-Gaussian expansion (MGE) method (Monnet et al. 1992; Emsellem et al. 1994), as implemented by Cappellari (2002)⁴.

Briefly, the MGE procedure starts by determining the galaxy’s average ellipticity, position angle, and coordinates of the luminosity-weighted center. The galaxy image is then divided in four quadrants, and a number of photometric profiles is measured along sectors uniformly spaced in angle from the major axis to the minor axis. Surface brightness profiles from sectors in the four quadrants are averaged together (an acceptable simplification for our galaxies since position angle and isophotal center do not show a significant radial dependency), and each is then fitted as the sum of Gaussian components. The best-fitting MGE model surface brightness is then determined iteratively by comparison with the observed surface brightness, after having been convolved with the instrumental PSF (generated, in our case, using the `TinyTIM` package, Krist & Hook 1999, and parametrized as the sum of circular Gaussians). The Gaussian width coefficients of the MGE model were constrained to be a set of logarithmically-spaced values, thus simplifying the fitting algorithm into a general non-negative least-squares problem for the corresponding Gaussian amplitudes. During the entire procedure, pixels for which correction for dust obscuration did not perform correctly

³Extinction in all relevant passbands are related to $A(V)$ as $A_{F435W}/A_V = 1.362$, $A_{F814W}/A_V = 0.597$, $A_{FR656N}/A_V = 0.781, 0.783$, and 0.805 for Abell 1836-BCG, Abell 2052-BCG, and Abell 3565-BCG, respectively (Cardelli et al. 1989; Schlegel et al. 1998).

⁴The code is publicly available at <http://www.strw.leidenuniv.nl/~mcappell/idl/>

(as in the case of Abell 2052-BCG) were masked.

The best-fitting MGE model (prior to PSF convolution) is then deprojected to a luminosity density $\Gamma(r)$ under the assumption that the galaxy is spherically symmetric – a justifiable simplification since the isophotes are nearly circular throughout the main body of our galaxies, including the radial range where the ionized-gas kinematics probes the galaxy potential (where however uncertainties are larger due to the presence of dust residuals, see Figures 5–7). For a radially-independent mass-to-light ratio, $(M/L)_*$, the stellar mass density $\rho(r)$ is then simply expressed as $\rho(r) = (M/L)_* \Gamma(r)$, and the stellar gravitational potential can be expressed in terms of error functions. The best-fitting, PSF-convolved MGE models to the observed surface-brightness profiles are shown in Figures 11–13, along with the deprojected luminosity density profiles (prior to PSF-convolution), and the corresponding circular velocity curves [for $(M/L)_* = 1$].

3.5. Ionized-gas distribution

Continuum-free emission-line images for the sample galaxies were obtained by subtracting the WFPC2/F814W images from the ACS/FR656N images which isolate the spectral region characterized by the redshifted H α and [N II] $\lambda\lambda 6548, 6583$ emission lines. All images were previously extinction corrected as described in § 3.3, after having been resampled and rotated in order to match the pixel scale and orientation of the lower-resolution WFPC2/F814W images. Before subtraction, the FR656N images were multiplied by a factor equal to the mean ratio between the F814W and resampled FR656N images, calculated in emission-free regions. The resulting emission line maps are shown in the central panels of Figures 8–10. The intrinsic (prior to PSF broadening) surface-brightness distribution of the ionized gas, a key input to our modeling, was obtained independently using both the iterative method based on the Lucy-Richardson algorithm (Richardson 1972; Lucy 1974) and the MGE method already described in § 3.4. According to van den Bosch & Emsellem (1998) the two methods give consistent results, however, one might be preferable to the other depending on the specifics of the images (e.g., signal-to-noise ratio S/N, presence of asymmetric features, etc.). Both methods employed the PSF generated using TINY TIM for the WFPC2/F814W images. The Lucy-Richardson algorithm, as implemented in the IRAF task LUCY, was found to give satisfactory results in the case of Abell 2052-BCG and Abell 3565-BCG, for which the method converged after only five and six iterations, respectively. In the case of Abell 1836-BCG, for which the emission-line images have lower S/N, LUCY produced unacceptable noise amplification before convergence could be reached, and the intrinsic emission-line distribution was therefore recovered using the MGE method. We

note that the latter failed to produce acceptable results for Abell 2052-BCG and Abell 3565-BCG, for which the distribution of the ionized gas is less symmetric, violating the four-fold symmetry required by the MGE algorithm. The deconvolved surface-brightness distributions of the emission line gas are shown in the right panels of Figures 8–10.

4. Observations, data reduction and analysis: STIS spectroscopy

The spectroscopic observations of the sample galaxies were carried out with STIS between 2003 August 16 and 2004 February 21 as part of program GO-9838. The G750M grating was used at the prime tilt in combination with the $0''.1 \times 52''$ slit for Abell 1836-BCG and Abell 2052-BCG, and the $0''.2 \times 52''$ slit for Abell 3565-BCG. The slit width was selected to ensure that the sphere of influence of the SBH estimated to reside in each galaxy (based on the $M_{\bullet} - \sigma$ and $M_{\bullet} - M_B$ relations) could be comfortably resolved, while at the same time allowing for reasonable throughput. The G750M grating covers the wavelength range from 6480 Å to 7050 Å, which includes the $H\alpha$, [N II] $\lambda\lambda 6548, 6583$, and [S II] $\lambda\lambda 6716, 6731$ emission lines. The dispersion is $0.56 \text{ \AA pixel}^{-1}$, and the instrumental resolution is 0.83 \AA (FWHM, corresponding to $\sigma_{\text{instr}} \simeq 16.0 \text{ km s}^{-1}$ at [N II] $\lambda 6583$) for the $0''.1 \times 52''$ slit, and 1.5 \AA ($\sigma_{\text{instr}} \simeq 30.5 \text{ km s}^{-1}$) for the $0''.2 \times 52''$ slit. The spatial scale of the 1024×1024 SITE CCD is $0''.05 \text{ pixel}^{-1}$.

For each target galaxy, spectra were taken at three different slit positions, the first crossing the nucleus of the galaxy, and two additional ones displaced by one slit width ($0''.1$ for Abell 1836-BCG and Abell 2052-BCG, and $0''.2$ for Abell 3565-BCG) on either side, perpendicularly to the slit axis. All slits were oriented along the photometric major axis. In the case of Abell 3565-BCG, for which the wider slit allowed for shorter exposure times, one spectrum was taken at each slit position. For Abell 1836-BCG and Abell 2052-BCG two spectra were taken at each location, the second shifted along the slit axis by four pixels to facilitate removal of bad pixels and other CCD defects. A 90 s tungsten lamp flat exposure was taken after each galaxy spectrum, to correct for the fringing affecting the STIS CCD at wavelengths longer than $\approx 7000 \text{ \AA}$. A log of the STIS observations can be found in Table 3.

The spectra were reduced using the IRAF/CALSTIS reduction pipeline maintained by STScI. The basic reduction steps included overscan subtraction, bias subtraction, dark subtraction, flatfield correction, wavelength calibration as well as correction for geometric distortion. Correction for fringing was performed with the IRAF/DEFRINGE task. In the case of Abell3565-BCG, for which only one spectrum is available at each slit location, cosmic ray events and hot pixels were removed using the task LACOS_SPEC (van Dokkum 2001). For the other two galaxies, the two spectra obtained at the same slit position were aligned

with IRAF/IMSHIFT using the center of the stellar-continuum radial profile as a reference, and then combined using IRAF/IMCOMBINE. Cosmic ray rejection was performed with the CRREJECT option in IMCOMBINE, additionally, pixels flagged by running LACOS_SPEC separately on each spectrum were also removed. The sky background was determined from the combined, calibrated spectra between 15" and 30" from the nucleus and then subtracted. Finally, individual spectra were extracted every 0".05 (corresponding to 1 pixel) up to $\approx 0".2$, 0".3, and 0".7 from the center for Abell 1836-BCG, Abell 2052-BCG, and Abell 3565-BCG, respectively. At larger radii, the decreasing intensity of the emission lines required binning in the spatial direction (see Table 4 and Figures 14–16 for details) to obtain a S/N of at least 10 at the peak of the [N II] $\lambda 6583$ emission line in the combined spectrum, a condition deemed necessary for an accurate measurement of the line kinematics (§4.1). The final spectra along the major and offset axes of the sample galaxies are plotted in Figures 14(b)–16(b).

The location of the slit relative to the galaxy center was checked using STIS images taken after acquisition of the target galaxies. A series of “synthetic” slits were extracted from the acquisition images by averaging four adjacent columns for Abell 1836-BCG and Abell 2052-BCG (corresponding to a 0".1-wide slit), and eight adjacent columns for Abell 3565-BCG (corresponding to a 0".2-wide slit) at the nominal slit orientation. The radial brightness profiles in each synthetic slit were then compared to the profiles obtained by collapsing the spectrum at the nuclear location along the wavelength direction. The best match was determined by minimizing the χ^2 of the difference between the light profile of the spectrum and the light profile extracted from the acquisition image. In all cases, the slits were found to be all positioned at the nominal locations.

4.1. Measurement of the emission lines

The ionized-gas kinematics were measured from the narrow [N II] $\lambda 6583$ line, the brightest of the lines detected in our spectra. This line is preferred to H α since the latter is more severely blended, and could be significantly affected by emission from circumnuclear star-forming regions (e.g., Verdoes Kleijn et al. 2000; Coccato et al. 2006).

The emission lines’ central wavelengths, FWHMs, and intensities were measured following Beifiori et al. (2008). The best-fitting Gaussian parameters were derived using a non-linear least-squares minimization based on the robust Levenberg-Marquardt method (e.g., Press et al. 1992) implemented by Moré et al. (1980). The actual computation

was done using the MPFIT algorithm⁵ implemented by C. B. Markwardt under the IDL⁶ environment.

Because the line profiles are assumed to be Gaussian, it was often necessary to include two components in order to reproduce the extended wings observed for several of the emission lines (most notably $H\alpha$ but, in some cases, also $[\text{N II}] \lambda\lambda 6548, 6583$ and $[\text{S II}] \lambda\lambda 6716, 6731$). Lines in the same doublet ($[\text{N II}]$ and $[\text{S II}]$) were assumed to have the same velocity and velocity width. A flux ratio of 1:2.967 was assumed for the two $[\text{N II}]$ lines, as dictated by atomic physics (e.g., Osterbrock 1989). The stellar continuum was approximated with a low-order polynomial.

The major axis spectrum of Abell 1836-BCG displays both a narrow and a broad $H\alpha$ line within the inner $0''.25$. The broad-line emission appears to be spatially extended, with FWHM of $0''.17$, compared to the typical FWHM of the STIS PSF ($\sim 0''.075$). Only the $-0''.1$ offset spectrum shows a broad $H\alpha$ component within the inner $0''.1$ (two rows), which possibly originates in the same nebular complex that gives rise to the broad-line emission observed along the central slit.

Only the major axis spectrum of Abell 3565-BCG displays broad-line emissions. Within the inner $0''.15$ the spectrum shows an $H\alpha$ component while from $0''.15$ to $0''.41$ it shows broad components in $H\alpha$, $[\text{N II}] \lambda\lambda 6548, 6583$, and $[\text{S II}] \lambda\lambda 6716, 6731$. The broad $H\alpha$ emission is spatially extended, with a FWHM of $0''.13$.

The major-axis and the $-0''.1$ offset spectra of Abell 2052-BCG show both narrow and broad components in $H\alpha$, $[\text{N II}] \lambda\lambda 6548, 6583$, and $[\text{S II}] \lambda\lambda 6716, 6731$ within the inner $0''.30$. The $0''.1$ offset spectrum shows all the broad components in the inner $0''.1$. The broad lines have a FWHM of $0''.10$ for $H\alpha$, $0''.12$ for the $[\text{N II}]$ doublet, $0''.18$ for $[\text{S II}] \lambda 6716$, and $0''.08$ for $[\text{S II}] \lambda 6731$ ($[\text{S II}]$ broad lines have the same radial extension). They appear to be less extended than for the other two galaxies, although still marginally resolved.

Figures 17–19 show the results of the multi-Gaussian fitting for the spectra extracted at the nuclear location, and at a location displaced, along the major axis, by ≈ 70 parsec ($0''.15$, $0''.10$, and $0''.25$ for Abell 1836-BCG, Abell 2053-BCG, and Abell 3565-BCG respectively).

Line-of-sight heliocentric velocities, velocity dispersions and line intensities measured from the $[\text{N II}] \lambda 6583$ line along the major and offset axes of the nuclear dust disks are plotted in Figures 14(c)–16(c) and listed in Table 4.

⁵The updated version of this code is available on <http://cow.physics.wisc.edu/~craigm/idl/idl.html>

⁶Interactive Data Language is distributed by Research System Inc.

4.2. Ionized-gas kinematics and dust morphology

In the remainder of this Section, we will comment briefly on the kinematics of each individual galaxy. Before doing so, we note that both Abell 1836-BCG and Abell 3565-BCG display regular and symmetric velocity fields, as suggested by the smoothness and regularity of the ionized-gas disks. In contrast, Abell 2052-BCG, which is characterized by a more irregular emission-line morphology, shows irregular kinematics.

Abell 1836-BCG. The rotation curve, velocity dispersion profile, and flux profile along the major axis are relatively regular (Figure 14c), which makes this object appealing for dynamical modelling. The rotation velocity increases rapidly within the inner $0''.1$, reaching approximately 200 km s^{-1} , and flattening at larger distances. The velocity dispersion peaks at about 370 km s^{-1} at the nuclear location, and declines on either side, although not symmetrically. The off-axis kinematics show a similar pattern.

Abell 2052-BCG. The dust distribution in this galaxy is somewhat irregular, with several filaments distributed in a spiral-like pattern (Figure 2). This lack of symmetry is reflected in the flux distribution of the ionized gas, which is also not symmetric with respect to the center (lower panels of Figure 15c), and in the $[\text{N II}] \lambda 6583$ kinematics, which could be measured out to about $0''.3$ from the center along each slit positions (Figure 15c). At the nuclear location, the maximum rotation velocity (200 km s^{-1}) is reached at $0''.05$, with the velocity decreasing on either side, while the velocity dispersion curve is more symmetric, reaching $\approx 500 \text{ km s}^{-1}$ at the nuclear location. The spectra flanking the nuclear spectra are characterized by similar velocity dispersion profiles, but very different rotation curves; in particular, almost no rotation is observed along the slit displaced by $0''.1$ to the South-East. Because of this lack of regularity in the gas kinematics, we are only able to place an upper limit on the SBH mass of Abell 2052-BCG (§6.3).

Abell 3565-BCG. The $[\text{N II}] \lambda 6583$ kinematics are measured within $0''.8$ from the center along all three slit locations (Figure 16(c)). Although the smooth and well defined dust disk in Abell 3565-BCG starts to tilt slightly at large radii from the center (Figure 3), such a warp is clearly visible, and presumably kinematically important, only beyond the region where the ionized-gas kinematics is measured. The major-axis rotation velocity has a steep gradient, increasing to approximately 250 km s^{-1} within $0''.1$. It remains approximately constant out to the last observed point along the approaching side, while it decreases to about 100 km s^{-1} for radii larger than $0''.5$ along the receding side. The velocity dispersion profile is fairly symmetric and strongly peaked, reaching $\approx 450 \text{ km s}^{-1}$ at the center. The offset axes show rather similar kinematics, although the line fluxes are rather different. The rotation velocity increases almost linearly with radius, up to $\approx 200 \text{ km s}^{-1}$ at $\approx 0''.3$ from the center, while the velocity dispersion remains fairly constant at 120 km s^{-1} . Like Abell

1836-BCG, Abell 3565-BCG is a promising candidate for dynamical modeling.

5. Observations, data reduction and analysis: Ground-based spectroscopy

Although not used in the dynamical analysis, large scale stellar kinematics are necessary to place measured SBH masses on the $M_{\bullet}-\sigma_c$ relation. Velocity dispersions measurements exist in the literature for Abell 2052-BCG and Abell 3565-BCG, but not for Abell 1836-BCG. Ground-based spectroscopic observations of Abell 1836-BCG were therefore carried out in service mode with the 3.5-m New Technology Telescope (NTT) at the European Southern Observatory (ESO) in La Silla (Chile) on 2007 May 20 and July 10 [DDT programme ID 279.B-5004(A), P.I. E. Dalla Bontà]. The NTT mounted the ESO Multi-Mode Instrument (EMMI) in red medium-dispersion spectroscopic (REMD) mode, using the grating No. 7 with 600 grooves mm^{-1} in first order with a $1.0 \text{ arcsec} \times 5.5 \text{ arcmin}$ slit. The detector was the No. 62 MIT/LL CCD with 2048×4096 pixels of $15 \times 15 \mu\text{m}^2$. After a 2×2 on-chip pixel binning it yielded a wavelength coverage between about 4546 \AA and 6096 \AA with a reciprocal dispersion of $0.83 \text{ \AA pixel}^{-1}$. The instrumental resolution was 2.5 \AA (FWHM) corresponding to $\sigma_{inst} \approx 55 \text{ km s}^{-1}$ at 5900 \AA . The spatial scale was $0.332 \text{ arcsec pixel}^{-1}$. We took three spectra of 2400 s along the major axis of the galaxy (PA= 54°). The integration time was split into three exposures to deal with cosmic rays. Spectra of six giant stars with spectral type ranging from G7III to K5III were obtained, to use as templates. Arc lamp spectra were taken before and after every exposure to allow an accurate wavelength calibration. The average seeing FWHM during the observing runs was 1.0 arcsec in May 20 and 1.1 arcsec in July 10, as measured by the ESO Differential Image Motion Monitor.

All spectra were bias subtracted, flatfield corrected, cleaned of cosmic rays, corrected for bad pixels and columns, and wavelength calibrated using standard IRAF routines. It was checked that the wavelength rebinning was done properly by measuring the difference between the measured and predicted wavelengths (Osterbrock et al. 1996) for the brightest night-sky emission lines in the observed spectral ranges. The spectra were co-added using the center of the stellar continuum as reference. The contribution of the sky was determined from the outermost $\sim 30 \text{ arcsec}$ and $\sim 60 \text{ arcsec}$ at the two edges of the resulting spectrum, respectively, and then subtracted. A one-dimensional sky-subtracted spectrum was obtained for each kinematical template star. Flux calibration was not performed.

The stellar velocity dispersion was measured from the galaxy absorption features present in the wavelength range including the Mg line triplet ($\lambda\lambda 5164, 5173, 5184 \text{ \AA}$) using the Fourier Correlation Quotient method (Bender 1990) as done in Corsini et al. (2007). HR7429 (K3III) was adopted as the kinematical template. The stellar velocity dispersion was measured

within an aperture of $1/8r_e$. It was then applied the correction of Jorgensen et al. (1995) to derive the velocity dispersion within a circular aperture of radius $1/8r_e$. The correction was negligible, because the stellar velocity dispersion profile shows constant values, within the errors, toward the center. The stellar velocity dispersion of Abell 1836-BCG within a circular aperture of size $1/8r_e$ (Table 1) resulted to be $\sigma_c = 309 \pm 11 \text{ km s}^{-1}$.

A consistent value ($\sigma_c = 308 \pm 10 \text{ km s}^{-1}$) was obtained by measuring the velocity dispersion with the Penalized Pixel-Fitting Method (Cappellari & Emsellem 2004) as done in Méndez-Abreu et al. (2008). The measurement of the velocity dispersion from spectra obtained in the Mg triplet region can be problematic for massive ellipticals, due to possible mismatch of the abundance ratios with those of the adopted stellar templates (e.g., Barth et al. 2003). To address this issue, the Mg region was masked out (Fig. 20). A lower value of $\sigma_c = 288 \pm 9 \text{ km s}^{-1}$ was found after applying the aperture correction, and this was adopted for Abell 1836-BCG.

6. Dynamical modeling

Modeling of gas dynamics from HST data has steadily improved since the first successful applications of the method (Harms et al. 1994; Ferrarese et al. 1996; Barth et al. 2001; Sarzi et al. 2001; Marconi et al. 2003). For this study, we will use the procedure described in Coccato et al. (2006), where a detailed description of the method can be found. Briefly, a synthetic velocity field is generated assuming that the ionized gas is moving in circular orbits under the combined gravitational potential of stars and SBH. The gas is assumed to be confined in an infinitesimally thin disk centered at the photometric center of the galaxy. The model is projected onto the plane of the sky for a given inclination of the gaseous disk, and then degraded to simulate the actual setup of the spectroscopic observations. The latter step includes accounting for the width and location (namely position angle and offset with respect to the center) of each slit, instrumental PSF and charge bleeding between adjacent pixels. The free parameters of the model are the mass M_\bullet of the SBH, the mass-to-light ratio $(M/L)_\star$ of the stellar component (which we give in the I -band), and the inclination i of the gaseous disk; both $(M/L)_\star$ and i are assumed to be radially invariant. Although i can be estimated from the minor-to-major axial ratio of the disk, which is easily measured from the images, previous studies (Ferrarese et al. 1996, 1999; Sarzi et al. 2001; Shapiro et al. 2006) have shown that slight warps are common. When the ionized-gas emission arises predominantly from the innermost region of the dust disk, it is therefore best to treat i as a free parameter. The location of the slits, as well as the surface brightness distribution of the ionized gas (derived as described in § 3.5) are treated as input. M_\bullet , $(M/L)_\star$, and i are

determined by finding the model parameters which produce the best match to the observed velocity curve, obtained by minimizing $\chi^2 = \sum (v - v_{mod})^2 / \delta^2(v)$ where $v \pm \delta(v)$ and v_{mod} are the observed and model velocity along the different slit positions, respectively.

It has been noted in a number of studies of the kinematics of gas disks (Ferrarese et al. 1996, 1998; van der Marel & van den Bosch 1998; Verdoes Kleijn et al. 2000, 2002, 2007) that the measured velocity dispersion of the emission lines greatly exceeds what is expected from instrumental broadening and radial variations in rotational velocity of the gas within a single slit element, and requires an intrinsic component of random motion. In our model, this is assumed to be described by a radial function of the form $\sigma(r) = \sigma_0 + \sigma_1 e^{-r/r_\sigma}$. In principle, the exact characterization of $\sigma(r)$ affects the recovered velocity field, and therefore σ_0 , σ_1 , and r_σ should be treated as free parameters in the model, along with M_\bullet , i , and $(M/L)_*$. In practice, however, previous studies (Verdoes Kleijn et al. 2000; Barth et al. 2001; Coccato et al. 2006) have found that σ_0 , σ_1 , and r_σ are fairly insensitive to the values of M_\bullet , i , and $(M/L)_*$.

We have run a set of preliminary models in order to find the shape of the intrinsic velocity dispersion profile that is required to match our data, within the typical range of our key model parameters. Specifically, we explored a reasonable grid of values for black hole mass, inclination, and stellar I -band mass-to-light ratio, finding for each combination of these parameters the values of σ_0 , σ_1 , and r_σ that minimized $\chi^2 = \sum (v - v_{mod})^2 / \delta^2(v) + \sum (\sigma - \sigma_{mod})^2 / \delta^2(\sigma)$ where $\sigma \pm \delta(\sigma)$ and σ_{mod} are the observed and the model velocity dispersion along the major axis. In our final modeling procedure we have then fixed σ_0 , σ_1 , and r_σ to the values that were found for the best of such preliminary models (see next Sections).

In the following, the results for each galaxy will be discussed separately.

6.1. Abell 1836-BCG

We explored a three-dimensional grid of models with $0 \leq M_\bullet \leq 3.6 \times 10^{10} M_\odot$ in $2.4 \times 10^8 M_\odot$ steps, $0^\circ \leq i \leq 90^\circ$ in 1° steps, and $0 \leq (M/L)_* \leq 33 (M/L)_\odot$ in $0.4 (M/L)_\odot$ steps. Within this range, the intrinsic velocity dispersion of the gas best able to reproduce the observables is $\sigma(r) = 12 + 204 e^{-r/0.1 \text{ kpc}} \text{ km s}^{-1}$. The model adopts three parameters to fit 28 data points (the values of the rotational velocity), for a total of 25 degrees of freedom. The best model fitting the observed rotation curve (given the intrinsic velocity dispersion profile given above) requires $M_\bullet = 3.61_{-0.50}^{+0.41} \times 10^9 M_\odot$, $i = 69.0_{-1.9}^{+1.7}^\circ$, and $(M/L)_* = 5.0_{-0.9}^{+1.8} (M/L)_\odot$ (in the I -band), where the errors on M_\bullet , i , and $(M/L)_*$, are quoted at the 1σ

confidence level. The model, which has $\chi^2 = 85.3$ and a reduced $\chi_r^2 = 3.4$, is compared to the observed spectrum and kinematics in Figure 21 and Figure 22, respectively.

The small-scale asymmetries present in the model rotation curve (most evident at the central position) are a direct consequence of using in the models the intrinsic, PSF-deconvolved H α + [NII] intensity map (bottom panel of Figure 22). The observed rotation curves are well reproduced in general; the slight mismatch observed at $r \sim 0''.1$ for the slit located on the North-West side ($-0''.1$) of the nucleus (Figure 22) might be due to the presence of a slight warp in the outer part of the gas disk, which is not reproducible within the model’s framework.

The inclination angle derived from modeling the kinematic data ($i = 69.0^{+1.7}_{-1.9}^\circ$), which extend only as far as $r \lesssim 0''.2$, is significantly different from the inclination angle suggested by the axial ratio of the outer edge ($r \approx 0''.5$) of the disk, $i = 46^\circ \pm 5^\circ$. This suggests the presence of a warped structure, although such a tilting does not need to extend to the innermost regions where the kinematics was measured, and effectively our images can not constrain the gas geometry.

Figures 23–25 show the 1σ , 2σ and 3σ confidence levels (following the $\Delta\chi^2$ variations expected for two free parameters, i.e., 2.30, 6.17 and 11.8, Press et al. 1992) in the two-dimensional space of two of the fitted parameters, where the third parameter is held fixed at the best fitted value listed above. Finally, Figure 26 shows 1σ , 2σ , and 3σ confidence levels individually on M_\bullet , i , and $(M/L)_*$, according to the $\Delta\chi^2$ variations expected for one parameter (i.e., 1, 4, and 9, Press et al. 1992), marginalizing over all other parameters.

6.2. Abell 3565-BCG

The rotation curves along the three slit positions, for a total of 90 velocity data-points, were fitted for a grid of model parameters defined by $0 \leq M_\bullet \leq 6.4 \times 10^9 M_\odot$ in $2.6 \times 10^7 M_\odot$ steps, $0^\circ \leq i \leq 90^\circ$ in 1° steps, and $0 \leq (M/L)_* \leq 12 (M/L)_\odot$ in $0.3 (M/L)_\odot$ steps. Within this range, the intrinsic velocity dispersion of the gas best able to reproduce the observables is $\sigma(r) = 122 + 98 e^{-r/0.01 \text{ kpc}} \text{ km s}^{-1}$. The best model, which has $\chi^2 = 1518$ and a reduced $\chi_r^2 = 17.5$ (for 87 degrees of freedoms), requires $M_\bullet = 1.34^{+0.21}_{-0.19} \times 10^9 M_\odot$, $i = 66.0^{+3.5}_{-3.4}^\circ$ and $(M/L)_* = 6.3^{+1.1}_{-1.0} (M/L)_\odot$, where all errors are given at the 1σ confidence level. Such formal uncertainties were conservatively estimated after scaling up our errors on the velocity measurement until $\chi_r^2 = 1$ (following Sarzi et al. 2001), acknowledging that our thin-disk model fails to reproduce some of the velocity structure observed in particular at the central and South-Eastern slit positions. Contrary to the case of Abell 1836-BCG, the

dynamical inclination angle of the disk is much closer to the morphological inclination angle, $i = 71^\circ \pm 1^\circ$, derived from the axial ratio of the outer edge of the disk ($r \approx 1''.4$). Although our kinematic data extend almost to this radius ($r \lesssim 0''.8$) in practice the luminosity weighting assigns more leverage to the data from the innermost region. The model is compared to the observed spectrum and kinematics in Figure 27 and Figure 28, respectively.

Figures 29–31 show the 1σ , 2σ , and 3σ confidence levels in the two-dimensional space of two of the fitted parameters, where the third parameter is held fixed at the best fitted value listed above. Figure 32 shows 1σ , 2σ , and 3σ confidence levels on M_\bullet , i , and $(M/L)_*$ alone, marginalizing over all other parameters. It is worth noticing that mass-to-light ratios derived by the models refer to the nucleus of the galaxy, and might differ from the stellar population characterizing the galaxy on larger scale.

6.3. Abell 2052-BCG

In the case of Abell 2052-BCG, the asymmetric nature of the gas kinematics (§4.2) prevents the application of the method described above to pinpoint M_\bullet . An upper limit on the SBH mass can however still be obtained as described in Sarzi et al. (2002). In brief, an upper limit can be derived under the assumption that the central [N II] $\lambda 6583$ emission-line width, σ , is produced by gas moving on circular orbits in a coplanar, randomly oriented disk in the Keplerian potential of the central black hole. If the line broadening is caused in part by non-gravitational forces, the derived upper-limit would well exceed the actual SBH mass.

The model was implemented under the assumption that the intrinsic radial flux profile of the gas can be described by a Gaussian:

$$F(r) = F_0 + F_1 \exp[-(r - r_0)^2 / 2\sigma_{flux}^2], \quad (4)$$

where the parameters F_0 , F_1 , r_0 , and σ_{flux} are derived by matching $F(r)$, after convolution with the STIS PSF, to the observed emission flux profile along the slit. For a given black-hole mass, and under the previous assumptions regarding the gas geometry and kinematics, the model produces two-dimensional projected maps for the moments of the line-of-sight velocity distribution (LOSVD) at any position (x, y) on the sky:

$$\overline{\Sigma v^k}(x, y) = \int \text{LOSVD}(x, y, v_z) v_z^k dv_z \quad (k = 0, 1, 2). \quad (5)$$

$\overline{\Sigma v^k}$ is then convolved with the STIS PSF; finally, the velocity dispersion, σ , which corresponds to $(\overline{\Sigma v^2} / \overline{\Sigma v^0} - (\overline{\Sigma v^1} / \overline{\Sigma v^0})^2)^{1/2}$, is extracted within a $0.05'' \times 0.1''$ aperture for comparison to the observables.

There is no information on the orientation of the gaseous disk within the central aperture, nor is it possible to estimate it by analyzing the dust morphology, which is irregular and does not show a disk-like structure. In principle, a lower-limit on the SBH mass can be estimated assuming an edge configuration, whereas a model with a perfectly face-on disk would allow for an infinite SBH mass. Fortunately such extreme configurations are statistically rare, and considering that randomly oriented disks have uniformly distributed $\cos i$ we can estimate 1σ upper and lower limits on M_\bullet by using models with $i = 33^\circ$ and $i = 81^\circ$, corresponding to $\cos i = 0.84$ and 0.16 , respectively. For each i , the SBH mass was varied in $0.1 \times 10^6 M_\odot$ steps between $6 \times 10^6 \leq M_\bullet \leq 11.0 \times 10^9 M_\odot$ until the observed gas velocity dispersion was matched. The models were run for three values of mass-to-light ratio: $(M/L)_\star=0$, $5.0 (M/L)_\odot$ (derived for Abell 1836-BCG), and 6.3 (as in the case of Abell 3565-BCG) $(M/L)_\odot$. The most conservative upper limit is obtained by neglecting altogether the stellar contribution to the gravitational potential, $(M/L)_\star=0$, giving $M_\bullet \leq 4.6 \times 10^9 M_\odot$ and $M_\bullet \leq 1.8 \times 10^9 M_\odot$ for $i = 33^\circ$ and $i = 81^\circ$ respectively. Consistent with Sarzi et al. (2002), adopting $(M/L)_\star=5.0$ or $6.3 (M/L)_\odot$, has very little effect: M_\bullet decreases slightly to $3.6 \times 10^9 M_\odot$ and $3.3 \times 10^9 M_\odot$ respectively for $i = 33^\circ$ and $9.8 \times 10^8 M_\odot$ and $7.7 \times 10^8 M_\odot$ respectively for $i = 81^\circ$. Figure 33 shows the dependence of M_\bullet on the assumed $(M/L)_\star$ for $i = 33^\circ$ and $i = 81^\circ$.

7. Discussion and conclusions

We have presented a dynamical analysis aimed at constraining the masses of the SBHs in three brightest cluster galaxies: Abell 1836-BCG, at a distance of 147.2 Mpc, Abell 2052-BCG, at a distance of 141.0 Mpc, and Abell 3565-BCG, at a distance of 50.8 Mpc. The models are based on data obtained with the Hubble Space Telescope. Broad-band WFPC2 and broad and narrow-band ACS images were used to constrain the luminosity profile and the distribution of the ionized gas, as traced by the $H\alpha + [N II]$ emission, while STIS was employed to measure the rotation velocity and velocity dispersion profiles, from the $[N II] \lambda 6583$ emission, along three parallel slits positions, the first aligned along the photometric major axis, and the others adjacent to the first on either side of the nucleus.

In the case of Abell 1836-BCG and Abell 3565-BCG, the regular morphology and kinematics observed for the ionized gas led to secure black hole mass detections of $M_\bullet = 3.61_{-0.50}^{+0.41} \times 10^9 M_\odot$ and $1.34_{-0.19}^{+0.21} \times 10^9 M_\odot$ (where the uncertainties represent 1σ errors⁷),

⁷Barth et al. 2001 show that the total error budget for gas-dynamical modelling is likely to be twice as large as such formal error estimates.

respectively. For Abell-2052-BCG, which displays irregular kinematics, an upper limit of $M_{\bullet} \leq 4.60 \times 10^9 M_{\odot}$ was derived under the conservative assumption of a negligible stellar contribution to the gravitational potential, and an inclination angle for the gas disk of 33° . At face value, the black hole in Abell 1836-BCG is the most massive to have been dynamically measured to-date.

In our modeling we have neglected the potential impact on our SBH mass determination of assigning a dynamical origin to the additional kinematic broadening that we have used in our models to match the observed profile for the gas velocity dispersion. Although it has been argued that this additional turbulence does not affect the bulk motion of the gas (e.g. van der Marel & van den Bosch 1998), it is important to notice that ignoring the possibility that the gas might be supported by dynamical pressure will lead to *under*-estimate the SBH mass. For instance, Barth et al. (2001) have shown that including a classical asymmetric drift correction led to an 12% increase of their best M_{\bullet} value. Unfortunately, we could not repeat this analysis in our models since the observed line-broadening exceeds by far the circular velocity, breaking down the epicyclic approximation on which the asymmetric drift correction is based. Nonetheless, our best SBH mass measurements are still likely to be underestimations of the real SBH mass.

Figure 34 shows the location of Abell 1836-BCG, Abell 2052-BCG, and Abell 3565-BCG in the $M_{\bullet}-\sigma_c$ (Ferrarese & Ford 2005; Tremaine et al. 2002) and near-infrared $M_{\bullet}-L_{bulge}$ (Graham 2007; Marconi & Hunt 2003) planes. *K*-band Two-Micron All-Sky Survey (2MASS) magnitudes were retrieved from the NASA/IPAC Infrared Science Archive, and corrected for Galactic extinction following Schlegel et al. (1998). Stellar velocity dispersions are from this paper (see §5) for Abell 1836-BCG, from Smith et al. (2000) in the case of Abell 3565-BCG (we adopt his high S/N measurement, $\sigma = 335 \pm 12 \text{ km s}^{-1}$), and Tonry (1985) for Abell 2052-BCG. We note that published estimates of σ for Abell 2052-BCG range between 250 km s^{-1} and 370 km s^{-1} ; the high end of this spread is probably due to contamination from a companion galaxy located only $8''$ away in the North-East direction. The contribution from this galaxy was explicitly accounted for by Tonry (1985), whose value, $\sigma = 253 \pm 12 \text{ km s}^{-1}$, we have adopted. Correcting the adopted values of σ to a circular aperture of size $1/8r_e$ (Table 1), following Jorgensen et al. (1995), we find $\sigma_c = 288 \pm 9 \text{ km s}^{-1}$, $\sigma_c = 233 \pm 11 \text{ km s}^{-1}$, and $\sigma_c = 322 \pm 12 \text{ km s}^{-1}$ for Abell 1836-BCG, Abell 2052-BCG and Abell 3565-BCG, respectively.

The SBH mass detected in Abell 3565-BCG, $M_{\bullet} = 1.34_{-0.19}^{+0.21} \times 10^9 M_{\odot}$, is consistent both with the $M_{\bullet}-\sigma_c$ (Ferrarese & Ford 2005) and the *K*-band $M_{\bullet}-L_{bulge}$ (Graham 2007) relations, which predict $M_{\bullet} = 1.7_{-0.9}^{+2.0} \times 10^9 M_{\odot}$ (the error is computed adopting a 0.34 dex scatter in M_{\bullet}) and $M_{\bullet} = 1.1_{-0.6}^{+1.1} \times 10^9 M_{\odot}$ (adopting a 0.30 dex scatter), respectively.

For Abell 2052-BCG, although the conservative upper limit on the black hole mass obtained for reasonable assumptions for $(M/L)_*$ and i (§5.3), is consistent with both the $M_\bullet - \sigma_c$ (Ferrarese & Ford 2005) and the K -band $M_\bullet - L_{bulge}$ (Graham 2007) relations, these predict significantly different masses, $3.5_{-1.9}^{+4.1} \times 10^8 M_\odot$ (adopting a 0.34 dex scatter) and $1.3_{-0.6}^{+1.3} \times 10^9 M_\odot$ (adopting a 0.30 dex scatter) respectively (but note the above caveat regarding the measurement of σ for this galaxy). Although the sense of the discrepancy is consistent with the one argued for by Lauer et al. (2007), the lack of a precise determination of the SBH mass in this galaxy prevents us from establishing which, if either, of the two relations better predicts M_\bullet in this case. The only two BCGs in the literature with a dynamically measured SBH mass are M87 (Macchetto et al. 1997) and NGC 1399 (Houghton et al. 2006). M87 appears to have a more massive black hole than expected based on its K -band luminosity while it obeys the $M_\bullet - \sigma_c$ relation. NGC 1399 is consistent with both the relations within their scatter.

Abell 1836-BCG appears to be an outlier in all SBH scaling relations. The dynamically measured SBH mass reported in this paper, $M_\bullet = 3.61_{-0.50}^{+0.41} \times 10^9 M_\odot$, is larger, at the 3σ level, than the value of $M_\bullet = 9.6_{-4.8}^{+9.5} \times 10^8 M_\odot$ (adopting a 0.30 dex scatter), predicted by the K -band $M_\bullet - L_{bulge}$ relation (Graham 2007). It is also larger, at the 3σ level, than the value of $M_\bullet = 9.77_{-5.30}^{+11.6} \times 10^8 M_\odot$ (adopting a 0.34 dex scatter), predicted by the $M_\bullet - \sigma_c$ relation of Ferrarese & Ford (2005). Finally, the SBH mass of Abell 1836-BCG is not consistent with the value of $M_\bullet = 6.3_{-4.1}^{+11.5} \times 10^8 M_\odot$ predicted by the fundamental plane relation for SBHs by Hopkins et al. (2007), adopting an effective radius $r_e = 13''.1 = 9.3$ kpc with a scatter of 0.45 dex in M_\bullet .

The existence of extremely massive SBHs as outliers to the empirical $M_\bullet - \sigma_c$ relation would not be surprising. As shown by Lauer et al. (2007), the $M_\bullet - L_{bulge}$ relation predicts a greater abundance of the most massive SBHs, given the luminosities of the BCGs and the lack of galaxies with velocity dispersions larger than ~ 350 km s $^{-1}$. At the same time, the observed luminosity function of AGN implies the presence of SBHs as massive as $\sim 5 \times 10^9 M_\odot$ within the distance of the clusters we have observed, and SBHs mergers can increase the highest SBH masses in these massive clusters up to $\sim 10^{10} M_\odot$ (Yoo et al. 2007). A larger sample of SBH masses measured in massive clusters would be required to test models of the effect of mergers in increasing the largest SBH masses in the universe.

In conclusion, both the $M_\bullet - \sigma_c$ and $M_\bullet - L_{bulge}$ relations appear at their high- M_\bullet end to be consistent with the SBH mass measured for one BCG, Abell 3565-BCG, but inconsistent with another one, Abell 1836-BCG. For the remaining target, Abell 2052-BCG, although the ionized-gas kinematics allowed us only to set an upper-limit on M_\bullet it seems unlikely that this galaxy could obey both relations simultaneously. The fact that Abell 1836-BCG is an

outliers in both the $M_{\bullet}-\sigma_c$ and $M_{\bullet}-L_{bulge}$ relations would appear to weaken the claim of Lauer et al (2007) that L_{bulge} is more reliable predictor of M_{\bullet} for BCGs. Overall, our results might indicate that the scatter of SBH scaling relations increases at the high end, although additional data are necessary to test this claim.

EDB acknowledges the Fondazione “Ing. Aldo Gini” for a research fellowship, the Herzberg Institute of Astrophysics, Victoria, BC, and the University of Oxford, UK, for the hospitality while this paper was in progress. JM is supported in part by Spanish grants AYA 2006-06341 and AYA2006-15623-C02-01. Support for program GO-9838 was provided through a grant from the Space Telescope Science Institute, which is operated by the Association of Universities for Research in Astronomy, Inc., under NASA contract NAS5-26555. We thank V. Debattista, R. Trotta, and M. Cappellari for the stimulating discussions.

REFERENCES

- Abell, G. O. 1958, ApJS, 3, 211
- Abell, G. O., Corwin, H. G., Jr., & Olowin, R. P. 1989, ApJS, 70, 1
- Baggett, S., et al. 2002, in HST WFPC2 Data Handbook, v. 4.0, ed. B. Mobasher, Baltimore, STScI
- Barth, A. J., Sarzi, M., Rix, H.-W., Ho, L. C., Filippenko, A. V., & Sargent, W. L. W. 2001, ApJ, 555, 685
- Barth, A. J., Ho, L. C., & Sargent, W. L. W. 2003, ApJ, 583, 134
- Batcheldor, D., Marconi, A., Merritt, D., Axon, D. J. 2007, ApJ, 663, L85
- Beifiori, A., Sarzi, M., Corsini, E. M., Dalla Bontà, E., Pizzella, A., Coccato, L., & Bertola, F. 2008, ApJ, submitted
- Bender, R., 1990, A&A, 229, 441
- Benson, A. J., Džanović, D., Frenk, C. S., & Sharples, R. 2007, MNRAS, 379, 841
- Bernardi, M., Hyde, J. B., Sheth, R. K., Miller, C. J., & Nichol, R. C. 2007, AJ, 133, 1741
- Binney, J., & Tabor, G. 1995, MNRAS, 276, 663
- Cappellari, M. 2002, MNRAS, 333, 400

- Cappellari, M., & Emsellem, E. 2004, *PASP*, 116, 138
- Cardelli, J. A., Clayton, G. C., & Mathis, J. S. 1989, *ApJ*, 345, 245
- Ciotti, L., & Ostriker, J. P. 2001, *ApJ*, 551, 131
- Coccatto, L., Sarzi, M., Pizzella, A., Corsini, E. M., Dalla Bontà, E., & Bertola, F. 2006, *MNRAS*, 366, 1050
- Corsini, E. M., Wegner, G., Saglia, R. P., Thomas, J., Bender, R., & Thomas, D. 2007, *ApJS*, in press (arXiv:0710.2190)
- Di Matteo, T., Colberg, J., Springel, V., Hernquist, L., & Sijacki, D. 2007, *ApJ*, submitted (arXiv:0705.2269)
- Emsellem, E., Monnet, G., & Bacon, R. 1994, *A&A*, 285, 723
- Ferrarese, L., van den Bosch, F. C., Ford, H. C., Jaffe, W., & O’Connell, R. W. 1994, *AJ*, 108, 1598
- Ferrarese, L., Ford, H. C., & Jaffe, W. 1996, *ApJ*, 470, 444
- Ferrarese, L. 2002, *ApJ*, 578, 90
- Ferrarese, L., & Ford, H. C. 1999, *ApJ*, 515, 583
- Ferrarese, L., & Merritt, D. 2000, *ApJ*, 539, L9
- Ferrarese, L., & Ford, H. 2005, *Space Science Reviews*, 116, 523
- Ferrarese, L., et al. 2006, *ApJS*, 164, 334
- Gebhardt, K., et al. 2000, *ApJ*, 539, L13
- Gebhardt, K., et al. 2003, *ApJ*, 583, 92
- Graham, A. W., Erwin, P., Caon, N., & Trujillo, I. 2001, *ApJ*, 563, L11
- Graham, A. W. 2007, *MNRAS*, 543
- Harms, R. J., et al. 1994, *ApJ*, 435, L35
- Heyer, I. et al. 2004, *WFPC2 Instrument Handbook*, Version 9.0 (Baltimore: STScI)
- Holtzman, J. A., Burrows, C. J., Casertano, S., Hester, J. J., Trauger, J. T., Watson, A. M., & Worthey, G. 1995, *PASP*, 107, 1065

- Ho, L. C., Sarzi, M., Rix, H.-W., Shields, J. C., Rudnick, G., Filippenko, A. V., & Barth, A. J. 2002, *PASP*, 114, 137
- Hopkins, P. F., Hernquist, L., Cox, T. J., Robertson, B., & Krause, E. 2007, *ApJ*, in press (arXiv:0707.4005)
- Houghton, R. C. W., Magorrian, J., Sarzi, M., Thatte, N., Davies, R. L., & Krajnović, D. 2006, *MNRAS*, 367, 2
- Hudson, M. J., Lucey, J. R., Smith, R. J., Schlegel, D. J., & Davies, R. L. 2001, *MNRAS*, 327, 265
- Jensen, J. B., Tonry, J. L., Barris, B. J., Thompson, R. I., Liu, M. C., Rieke, M. J., Ajhar, E. A., & Blakeslee, J. P. 2003, *ApJ*, 583, 712
- Jedrzejewski, R. I. 1987, *MNRAS*, 226, 747
- Jorgensen, I., Franx, M., & Kjaergaard, P. 1995, *MNRAS*, 276, 1341
- Khochfar, S., & Silk, J. 2006, *ApJ*, 648, L21
- Kormendy, J., Richstone, D. 1995, *ARA&A*, 33, 581
- Kriss, G. 1994, In: *Astronomical Data Analysis Software and Systems III*, eds. D. R. Crabtree, R. J. Hanisch, and J. Barnes, *ASP Conf. Ser.*, 61, 437 (San Francisco: ASP)
- Krist, J., Hook, R., 1999, *The Tiny Tim User's Guide* (Baltimore: STScI)
- Laine, S., van der Marel, R. P., Lauer, T. R., Postman, M., O'Dea, C. P., & Owen, F. N. 2003, *AJ*, 125, 478
- Lauer, T. R., et al. 1995, *AJ*, 110, 2622
- Lauer, T. R., et al. 2007, *ApJ*, 662, 808
- Lucy, L. B. 1974, *AJ*, 79, 745
- Macchetto, F., Marconi, A., Axon, D. J., Capetti, A., Sparks, W., & Crane, P. 1997, *ApJ*, 489, 579
- Maciejewski, W., & Binney, J. 2001, *MNRAS*, 323, 831
- Marconi, A., & Hunt, L. K. 2003, *ApJ*, 589, L21
- Marconi, A., et al. 2003, *ApJ*, 586, 868

- Marconi, A., Risaliti, G., Gilli, R., Hunt, L. K., Maiolino, R., & Salvati, M. 2004, *MNRAS*, 351, 169
- Méndez-Abreu, J., Corsini, E. M., Debattista, V. P., De Rijcke, S., Aguerri, J. A. L., & Pizzella, A. 2008, *ApJ*, 679, L73
- Monnet, G., Bacon, R., & Emsellem, E. 1992, *A&A*, 253, 366
- Moré, J. J., Garbow, B. S., & Hillstom, K. E. 1980, User guide for MINPACK-1, Report ANL-80-74 (Argonne: Argonne National Laboratory)
- Osterbrock, D. E. 1989, *Astrophysics of Gaseous Nebulae and Active Galactic Nuclei* (Mill Valley: University Science Books)
- Osterbrock, D. E., Fulbright, J. P., Martel, A. R., et al. 1996, *PASP*, 108, 277
- Pavlovsky, C., et al. 2004a, *ACS Instrument Handbook, Version 5.0* (Baltimore: STScI)
- Pavlovsky, C., et al. 2004b, *ACS Data Handbook, Version 3.0*, (Baltimore: STScI).
- Postman, M., & Lauer, T. R. 1995, *ApJ*, 440, 28
- Press, W. H., Teukolsky, S. A., Vetterling, W. T., & Flannery, B. P. 1992, *Numerical Recipes in Fortran 77* (Cambridge: Cambridge University Press)
- Rest, A., van den Bosch, F. C., Jaffe, W., Tran, H., Tsvetanov, Z., Ford, H. C., Davies, J., & Schafer, J. 2001, *AJ*, 121, 2431
- Richardson, W. H. 1972, *J. Opt. Soc. Am.*, 62, 55
- Sarzi, M., Rix, H.-W., Shields, J. C., Rudnick, G., Ho, L. C., McIntosh, D. H., Filippenko, A. V., & Sargent, W. L. W. 2001, *ApJ*, 550, 65
- Sarzi, M., et al. 2002, *ApJ*, 567, 237
- Schawinski, K., et al. 2006, *Nature*, 442, 888
- Schlegel, D. J., Finkbeiner, D. P., & Davis, M. 1998, *ApJ*, 500, 525
- Shankar, F., Salucci, P., Granato, G. L., De Zotti, G., & Danese, L. 2004, *MNRAS*, 354, 1020
- Shapiro, K. L., Cappellari, M., de Zeeuw, T., McDermid, R. M., Gebhardt, K., van den Bosch, R. C. E., & Statler, T. S. 2006, *MNRAS*, 370, 559

- Sheth, R. K., et al. 2003, *ApJ*, 594, 225
- Sirianni, M., et al. 2005, *PASP*, 117, 1049
- Smith, R. J., Lucey, J. R., Hudson, M. J., Schlegel, D. J., & Davies, R. L. 2000, *MNRAS*, 313, 469
- Springel, V., Di Matteo, T., & Hernquist, L. 2005, *MNRAS*, 361, 776
- Suchkov, A. A., Berman, V. G., Heckman, T. M., & Balsara, D. S. 1996, *ApJ*, 463, 528
- Tonry, J. L. 1985, *AJ*, 90, 2431
- Tremaine, S., et al. 2002, *ApJ*, 574, 740
- Tundo, E., Bernardi, M., Hyde, J. B., Sheth, R. K., & Pizzella, A. 2007, *ApJ*, 663, 53
- van den Bosch, F. C., & Emsellem, E. 1998, *MNRAS*, 298, 267
- van der Marel, R. P., & van den Bosch, F. C. 1998, *AJ*, 116, 2220
- van der Marel, R. P., Cretton, N., de Zeeuw, P. T., & Rix, H.-W. 1998, *ApJ*, 493, 613
- Verdoes Kleijn, G. A., van der Marel, R. P., Carollo, C. M., & de Zeeuw, P. T. 2000, *AJ*, 120, 1221
- Verdoes Kleijn, G. A., van der Marel, R. P., de Zeeuw, P. T., Noel-Storr, J., & Baum, S. A. 2002, *AJ*, 124, 2524
- Verdoes Kleijn, G. A., van der Marel, R. P., & Noel-Storr, J. 2007, *AJ*, in press (arXiv:astro-ph/0601023)
- Vestergaard, M. 2004, *ApJ*, 601, 676
- von der Linden, A., Best, P. N., Kauffmann, G., & White, S. D. M. 2007, *MNRAS*, 379, 867
- Willott, C. J., McLure, R. J., & Jarvis, M. J. 2003, *ApJ*, 587, L15
- Yoo, J., Miralda-Escudé, J., Weinberg, D. H., Zheng, Z., & Morgan, C. W. 2007, *ApJ*, 667, 813

Table 1: Basic parameters of the sample galaxies

Galaxy	Other name	Type	D_{25}	r_e	m_B	m_K	cz	D	σ_c
(1)	(2)	[RC3] (3)	[arcmin] (4)	[arcsec] (5)	[mag] (6)	[mag] (7)	[km s ⁻¹] (8)	[Mpc] (9)	[km s ⁻¹] (10)
Abell 1836-BCG	PGC 49940	SA0 ⁻ :	1.4	13.10 ^a	14.56 ± 0.14 ^a	9.99 ± 0.04	11036	147.2	288 ± 9 ^a
Abell 2052-BCG	UGC 9799	E	1.8	55.98 ^b	14.4 ± 0.03 ^b	9.55 ± 0.06	10575	141.0	233 ± 11 ^b
Abell 3565-BCG	IC 4296	E	3.4	41.41 ^a	11.61 ± 0.05 ^c	7.50 ± 0.02	3834	50.8	322 ± 12 ^c

Note. — Col. (1): Galaxy name from Abell (1958) and Abell et al. (1989). Col. (2): Alternative identification. Col. (3): Morphological classification from RC3. Col. (4): Apparent major isophotal diameter measured at the surface brightness level $\mu_B = 25$ mag arcsec⁻² from RC3. Col. (5): Effective radius (a: from RC3, b: from Hudson et al. 2001). Col. (6): Total apparent B -band magnitude (a, c: from RC3, b: from Postman & Lauer 1995). Col. (7): Total apparent K -band magnitude from 2MASS. Col. (8): Systemic velocities in the frame of the Cosmic Microwave Background, from Laine et al. (2003) Col. (9): Distances from systemic velocity and $H_0 = 75$ km s⁻¹ Mpc⁻¹, except for Abell 3565-BCG (Jensen et al. 2003). Col. (10): Stellar velocity dispersion (a: this paper; b: Smith et al. 2000; c: Tonry 1985) corrected to a circular aperture of size $1/8r_e$.

Table 2: Log of the ACS and WFPC2 observations.

Galaxy	Filter	Pivot λ Å	Width Å	Exp. Time [s]	Obs. Date
(1)	(2)	(3)	(4)	(5)	(6)
ACS					
Abell 1836-BCG	F435W	4311	310	2×895.0	2004 Feb 20
	FR656N	6803	136	2×1382.5	2004 Feb 20
Abell 2052-BCG	F435W	4311	310	2×900.0	2003 Sep 3
	FR656N	6788	136	2×1380.0	2003 Sep 3
Abell 3565-BCG	F435W	4317	293	2×900.0	2004 Aug 7
	FR656N	6645	133	2×1388.0	2004 Aug 7
WFPC2					
Abell 1836-BCG	F814W	8012	1539	2×500.0	2001 Apr 11
Abell 2052-BCG	F814W	8012	1539	2×500.0	2001 Apr 17
Abell 3565-BCG	F814W	8012	1539	$1 \times 900.0 + 5 \times 1100.0 + 4 \times 1300.0$	1996 Jan 19-20

Note. — Col. (1): Galaxy name. Col. (2): Filter name. Col. (3): Pivot wavelength (ACS: Sirianni et al. 2005; WFPC2: Heyer et al. 2004). Col. (4): Filter width (ACS: Sirianni et al. 2005; WFPC2: Heyer et al. 2004). Col. (5): Total exposure time. Col. (6): Observation date.

Table 3: Log of the STIS observations.

Galaxy	Offset	PA	Exp. Time	Obs. Date
(1)	["]	[°]	[s]	(5)
	0.0	−127.9	2040 + 2800	2004 Feb 21
Abell 1836-BCG	−0.1	−127.9	2 × 2800	2004 Feb 21
	+0.1	−127.9	2 × 2800	2004 Feb 21
	0.0	51.0	2030 + 2800	2003 Sept 2
Abell 2052-BCG	−0.1	51.0	2 × 2800	2003 Sept 2
	+0.1	51.0	2 × 2800	2003 Sept 2
	0.0	75.4	2010	2003 Aug 16
Abell 3565-BCG	−0.2	75.4	2735	2003 Aug 16
	+0.2	75.4	2735	2003 Aug 16

Note. — Col. (1): Galaxy name. Col. (2): Measured offset of the slit center with respect to the galaxy nucleus. Col. (3): Position angle of the slit, measured from north to east. Col. (4): Total exposure time. Col. (5): Observation date.

Table 4. [N II] $\lambda 6583$ kinematics.

r [""] (1)	V [km s ⁻¹] (2)	σ [km s ⁻¹] (3)	r [""] (4)	V [km s ⁻¹] (5)	σ [km s ⁻¹] (6)	r [""] (7)	V [km s ⁻¹] (8)	σ [km s ⁻¹] (9)
Abell 1836-BCG								
+0'.1 offset			major axis			-0'.1 offset		
-0.23	11382± 25	80 ± 28	-0.23	11500 ± 28	165 ± 27	-0.23	11418 ± 24	133± 24
-0.18	11398± 51	256 ± 52	-0.18	11422 ± 31	289 ± 31	-0.18	11361 ± 17	137± 18
-0.13	11402± 53	369 ± 51	-0.13	11455 ± 18	266 ± 22	-0.13	11341 ± 18	200± 18
-0.08	11288± 26	306 ± 27	-0.08	11413 ± 11	294 ± 13	-0.08	11283 ± 18	275± 19
-0.03	11307± 19	286 ± 20	-0.03	11369 ± 11	370 ± 13	-0.03	11237 ± 30	396± 38
0.02	11199± 17	228 ± 17	0.02	11118 ± 13	362 ± 17	0.02	11094 ± 35	260± 31
0.07	11202± 43	346 ± 45	0.07	11001 ± 13	208 ± 17	0.07	11082 ± 30	301± 43
0.12	11094± 21	132 ± 22	0.12	10993 ± 11	114 ± 12	0.12	11024 ± 60	241± 64
0.17	11091± 28	164 ± 29	0.17	10978 ± 20	123 ± 21			
0.22	11014± 14	51 ± 19	0.22	10982 ± 21	92 ± 23			
Abell 2052-BCG								
+0'.1 offset			major axis			-0'.1 offset		
-0.25	10189± 27	103 ± 28	-0.30	10172± 56	209± 56	-0.30	10100 ± 17	83± 18
-0.20	10220± 39	229 ± 37	-0.25	10156± 34	179± 31	-0.25	10011 ± 33	213± 30
-0.15	10247± 17	158 ± 16	-0.20	10130± 17	183± 17	-0.20	9979 ± 13	193± 13
-0.10	10318± 16	169 ± 16	-0.15	10160± 15	176± 23	-0.15	9912 ± 11	102± 15
-0.05	10330± 8	132 ± 9	-0.10	10154± 10	171± 16	-0.10	9908 ± 7	186± 9
0.00	10329± 11	169 ± 12	-0.05	10220± 9	150± 13	-0.05	9930 ± 7	199± 9
0.0	10348± 15	211 ± 15	0.00	10436± 18	294± 20	0.00	10075 ± 12	168± 16
0.10	10312± 23	236 ± 22	0.05	10494± 23	190± 28	0.05	10186 ± 25	215± 29
0.15	10311± 16	176 ± 15	0.10	10364± 19	187± 21	0.10	10242 ± 26	162± 35
0.20	10311± 22	132 ± 22	0.15	10251± 23	199± 21	0.15	10236 ± 16	147± 16
0.25	10313± 21	97 ± 21	0.20	10251± 16	133± 16	0.20	10242 ± 21	191± 21
0.30	10328± 29	194 ± 29	0.25	10263± 12	83 ± 13	0.25	10296 ± 15	73± 16
0.36	10268± 22	97 ± 23	0.30	10301± 30	138± 30			
0.41	10459± 35	109 ± 36	0.36	10293± 88	159± 89			
0.46	10312± 14	38 ± 19	0.46	10293± 32	113± 33			
Abell 3565-BCG								
+0'.1 offset			major axis			-0'.1 offset		
-0.76	4018± 20	86± 23	-0.81	4011 ± 13	62± 16	-0.71	4015± 26	135 ± 27
-0.71	4010± 11	80± 12	-0.71	4045 ± 24	133± 25	-0.61	4054± 18	86 ± 21
-0.66	4020± 11	97± 12	-0.66	4073 ± 16	113± 17	-0.56	3999± 11	69 ± 13
-0.61	4046± 12	115± 13	-0.61	4057 ± 14	88± 16	-0.51	4006± 16	112 ± 17
-0.56	4032± 9	107± 9	-0.56	4064 ± 13	100± 14	-0.46	4017± 15	113 ± 16
-0.51	4057± 10	132± 11	-0.51	4102 ± 16	119± 17	-0.41	3987± 15	120 ± 16
-0.46	4077± 12	154± 12	-0.46	4101 ± 15	117± 16	-0.36	3976± 13	110 ± 14
-0.41	4073± 11	142± 12	-0.41	4085 ± 14	111± 15	-0.30	3970± 12	97 ± 13
-0.36	4054± 13	177± 12	-0.36	4099 ± 13	143± 14	-0.25	3954± 8	82 ± 10
-0.30	4028± 12	181± 12	-0.30	4116 ± 16	193± 16	-0.20	3939± 8	107 ± 9
-0.25	4032± 13	213± 14	-0.25	4125 ± 12	206± 12	-0.15	3898± 9	147 ± 10
-0.20	4016± 10	224± 10	-0.20	4077 ± 9	204± 10	-0.10	3866± 6	115 ± 7

Table 4—Continued

r [$''$] (1)	V [km s^{-1}] (2)	σ [km s^{-1}] (3)	r [$''$] (4)	V [km s^{-1}] (5)	σ [km s^{-1}] (6)	r [$''$] (7)	V [km s^{-1}] (8)	σ [km s^{-1}] (9)
−0.15	3970± 8	227± 9	−0.15	4068 ± 19	226± 14	−0.05	3833± 5	112 ± 6
−0.15	3971± 8	234± 8	−0.10	4116 ± 15	251± 15	0.00	3824± 4	109 ± 4
−0.10	3926± 5	206± 5	−0.05	4084 ± 17	399± 18	0.05	3815± 4	97 ± 4
−0.05	3874± 4	191± 4	0.00	3830 ± 13	451± 16	0.10	3804± 4	99 ± 5
0.00	3818± 3	155± 3	0.05	3673 ± 6	254± 8	0.15	3746± 15	195 ± 15
0.05	3791± 3	138± 3	0.10	3607 ± 6	203± 8	0.20	3725± 12	167 ± 12
0.10	3762± 5	164± 5	0.15	3590 ± 8	171± 10	0.25	3681± 16	176 ± 17
0.15	3729± 8	201± 8	0.20	3572 ± 14	149± 15	0.30	3685± 16	134 ± 16
0.20	3686± 9	204± 9	0.25	3599 ± 8	181± 8	0.36	3669± 17	155 ± 17
0.25	3655± 11	165± 11	0.30	3551 ± 11	166± 11	0.41	3629± 22	163 ± 23
0.30	3652± 10	150± 10	0.36	3551 ± 14	179± 14	0.46	3670± 19	168 ± 20
0.36	3648± 9	130± 9	0.41	3583 ± 23	260± 23	0.51	3650± 19	130 ± 20
0.41	3636± 8	96± 9	0.46	3566 ± 22	195± 23	0.56	3685± 11	81 ± 12
0.46	3621± 10	120± 11	0.51	3523 ± 37	195± 37	0.61	3659± 13	99 ± 15
0.51	3588± 14	140± 15	0.56	3583 ± 40	216± 41	0.66	3672± 21	150 ± 22
0.56	3582± 13	149± 14	0.61	3495 ± 22	119± 23	0.71	3629± 17	85 ± 19
0.61	3595± 11	109± 12	0.66	3481 ± 26	94± 29	0.76	3671± 16	68 ± 20
0.66	3622± 13	101± 14	0.76	3552 ± 29	119± 31			
0.71	3624± 18	94± 20						

Note. — Col. (1)-(3): Galactocentric distance, line-of-sight heliocentric velocity (uncorrected for inclination), and line-of-sight velocity dispersion (uncorrected for instrumental velocity dispersion) measured from the [NII] λ 6583 line in the +0 $''$.1 offset spectrum. Col. (4)-(6): As in Col. (1)-(3) but for the major-axis spectrum. Col. (7)-(9): As in Col. (1)-(3) but for the −0 $''$.1 offset spectrum.

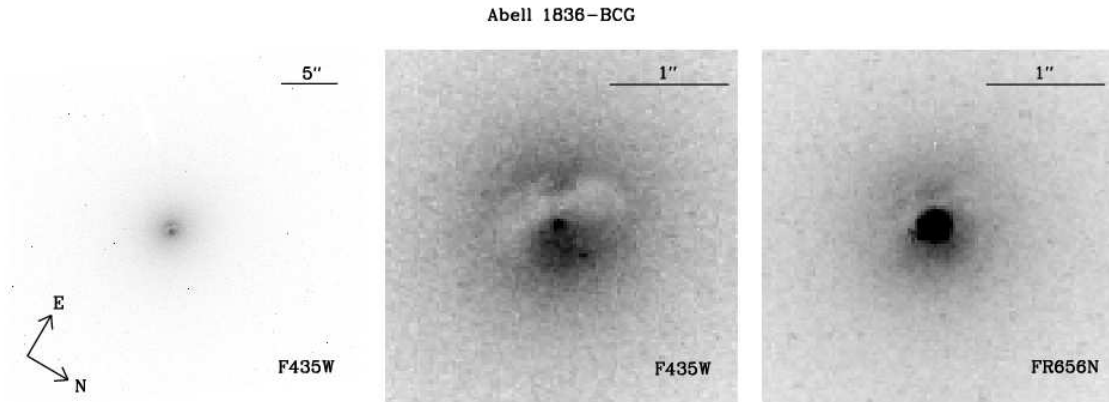


Fig. 1.— ACS/HRC images of Abell 1836-BCG. The *panels* show the F435W full frame (*left*) and a zoom toward the center (*center*). The same central section is shown in the *right panel* for the FR656N image. The grey-scale used for the left panel (full frame) is kept the same in Figures 1-3, while the gray-scale for the other panels changes from filter to filter in order to highlight the distribution of the nuclear dust. All images have been background subtracted.

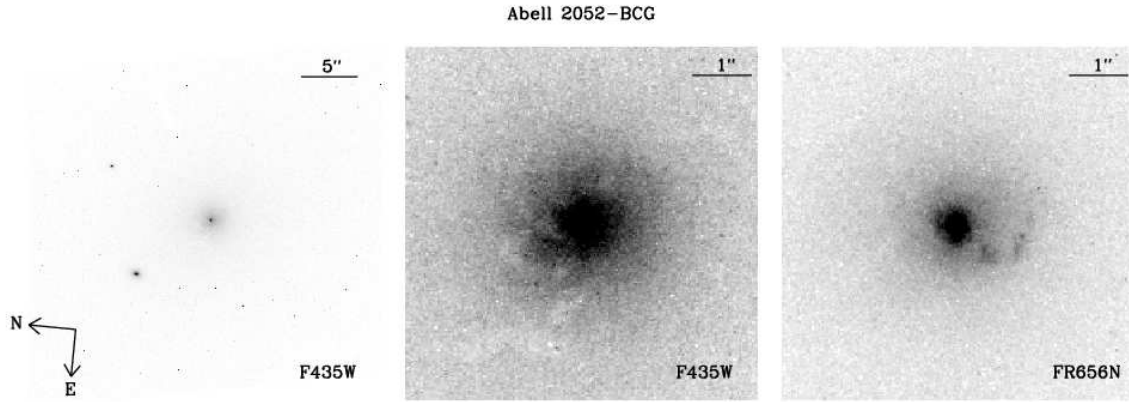


Fig. 2.— ACS/HRC images of Abell 2052-BCG. See Figure 1 for details.

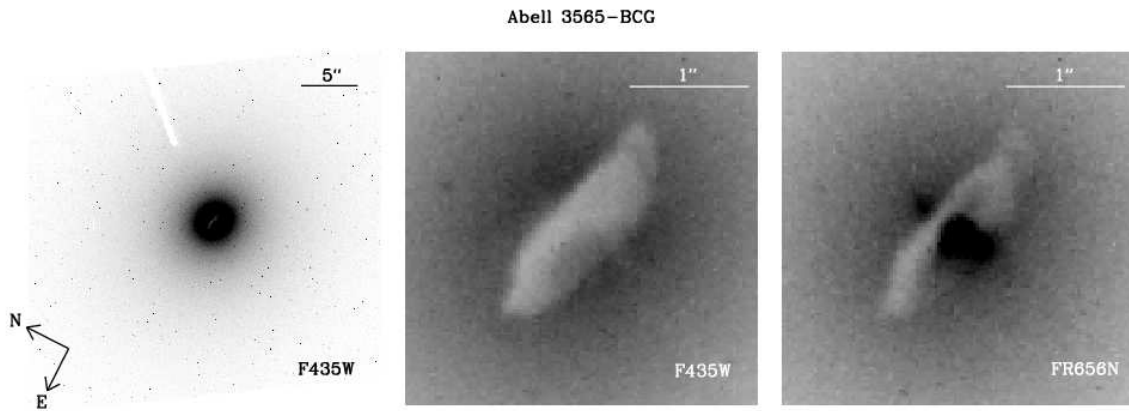


Fig. 3.— ACS/HRC images of Abell 3565-BCG. See Figure 1 for details.

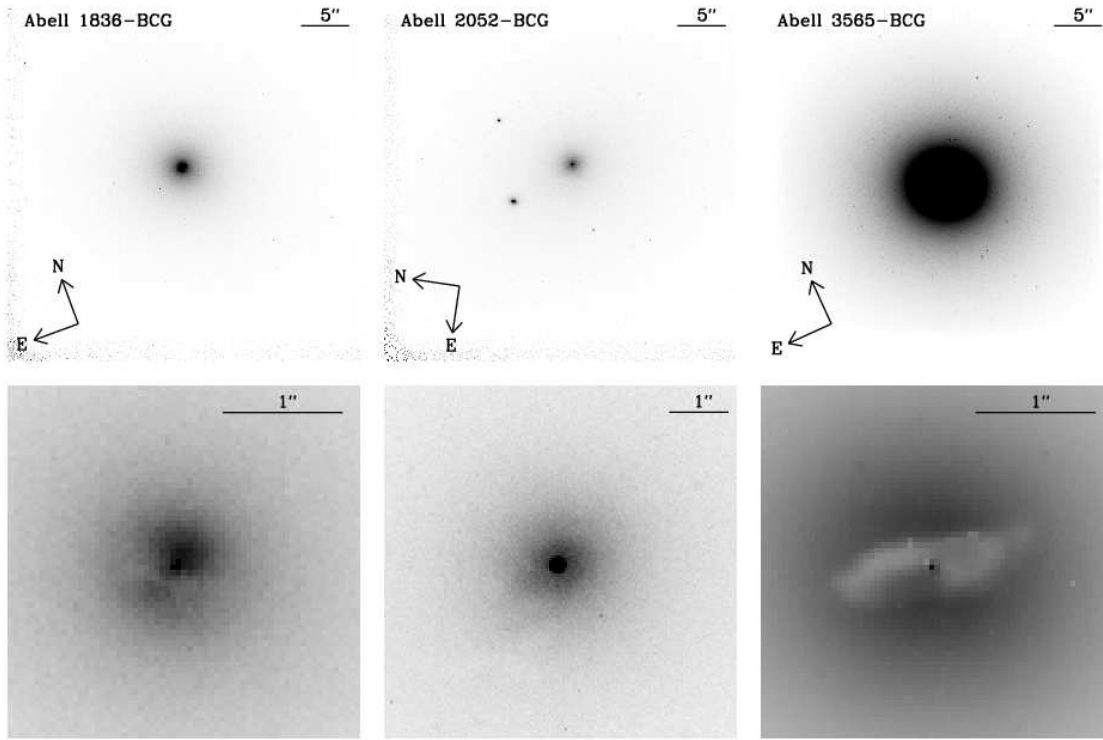


Fig. 4.— WFPC2/F814W images of Abell 1836-BCG (*left panels*), Abell 2052-BCG (*middle panels*), and Abell 3565-BCG (*right panels*). The *top panels* show the full frame, while the *bottom panels* show a zoom toward the center. The grey-scale used for the top (full frame) images is kept the same for all the three galaxies, while the gray-scale for the central sections changes from galaxy to galaxy to highlight the distribution of the nuclear dust. All images have been background subtracted.

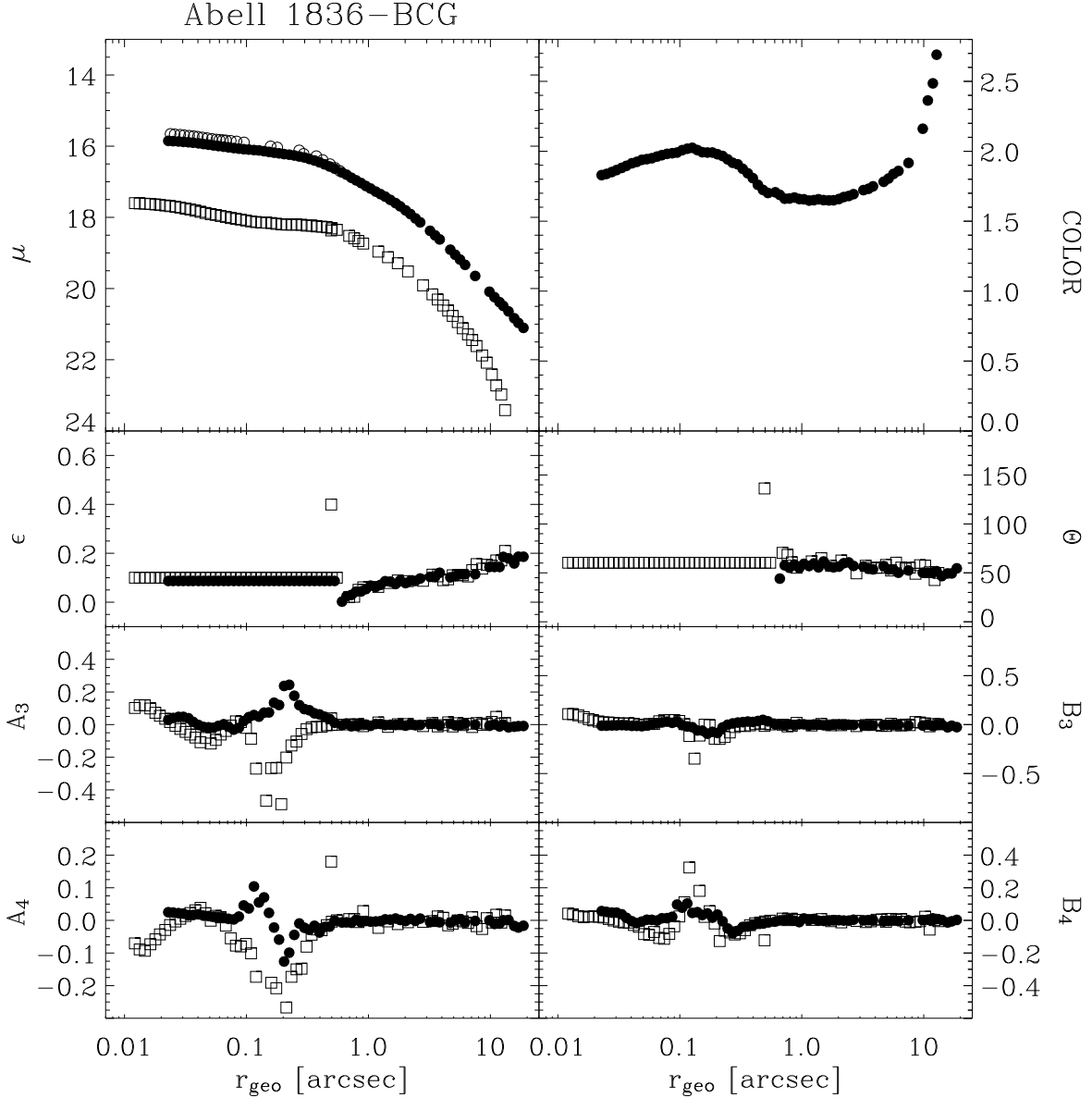


Fig. 5.— Isophotal parameters for Abell 1836-BCG plotted against the “geometric mean” radius $r_{geo} = a(1 - \epsilon)^{1/2}$, with a measured along the semimajor axis of the galaxy. The panels show the radial profiles of: surface brightness μ (in mag arcsec $^{-2}$) in ACS/F435W (squares) and WFPC2/F814W (filled circles) bands, F435W–F814W (filled circles) color, ellipticity ϵ , position angle θ (in degrees, measured from north to east), and parameters A_3 , A_4 , B_3 , and B_4 , measuring deviations of the isophotes from pure ellipses (see text for details). Open circles show the inner radial profile of μ measured on the WFPC2/F814W image corrected for dust obscuration (as described in the text) with the addition of the Galactic extinction correction by Schlegel et al. (1998).

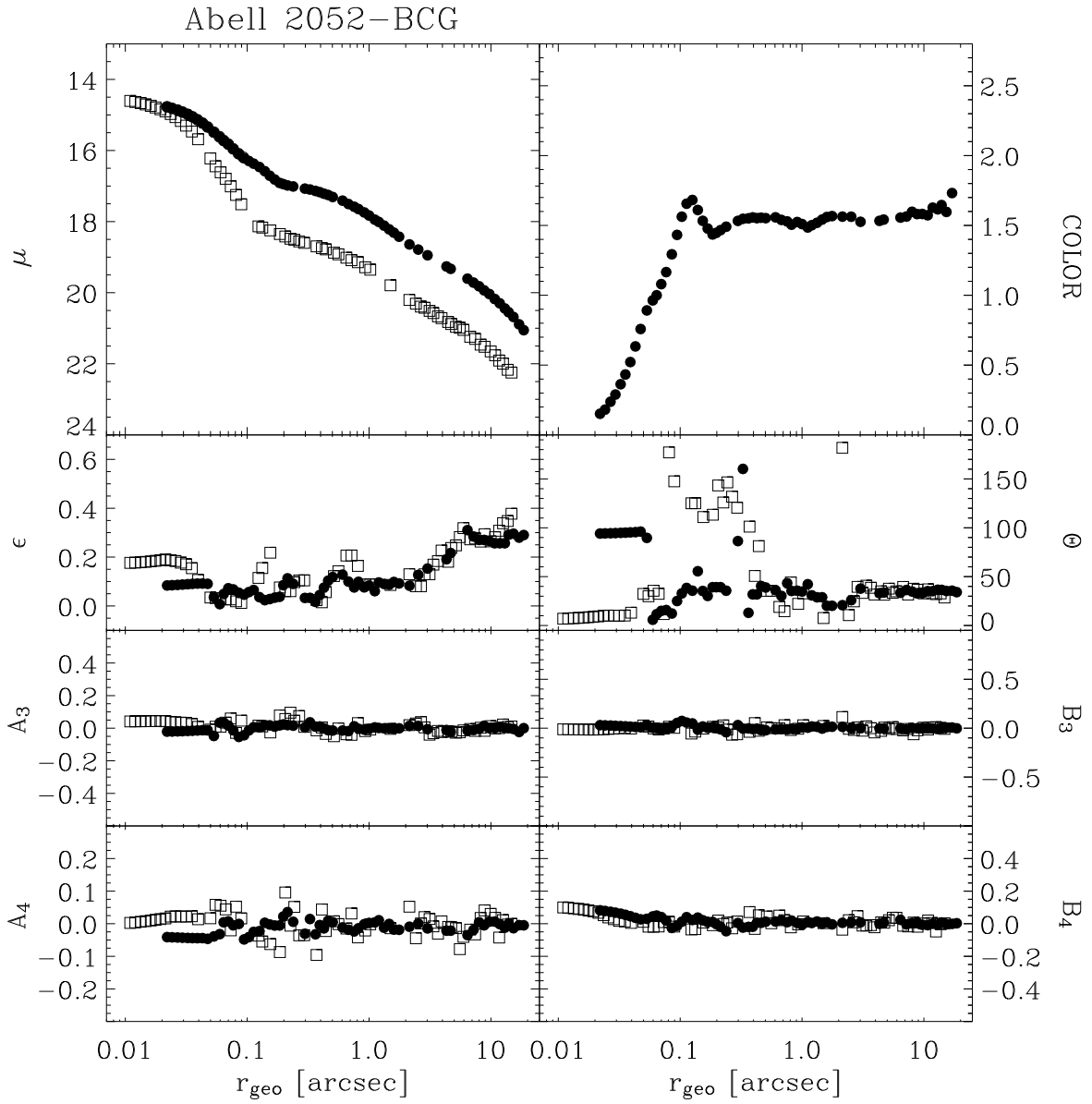


Fig. 6.— The same as for Figure 5, but for Abell 2052-BCG.

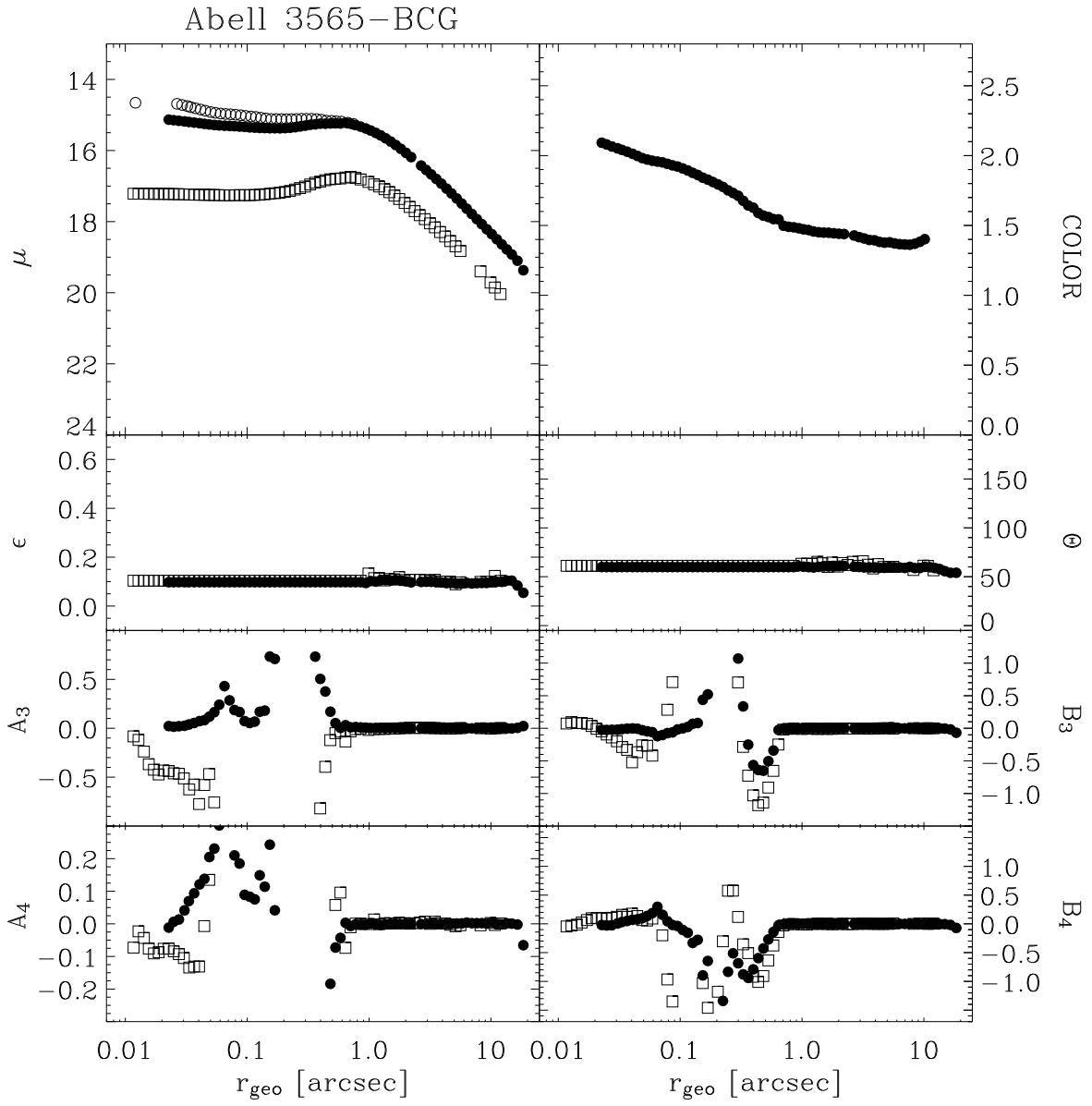


Fig. 7.— The same as for Figure 5, but for Abell 3565-BCG.

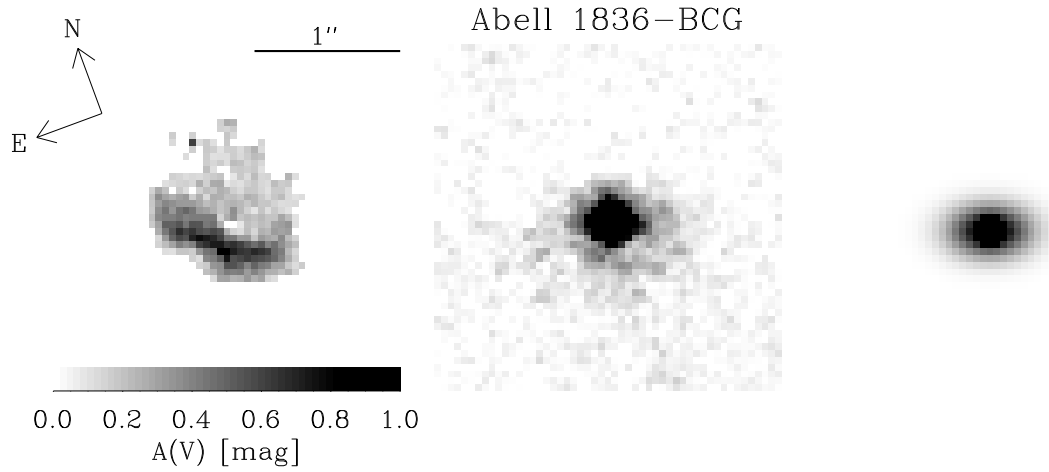


Fig. 8.— Optical depth map of Abell 1836-BCG (*left panel*), and continuum-subtracted emission-line images in the ACS/FR656N band pass before (*central panel*) and after deconvolution (*right panel*). The field of view is $6''.9 \times 6''.9$. Orientation and scale are given in the left panel and they are kept the same for all the panels.

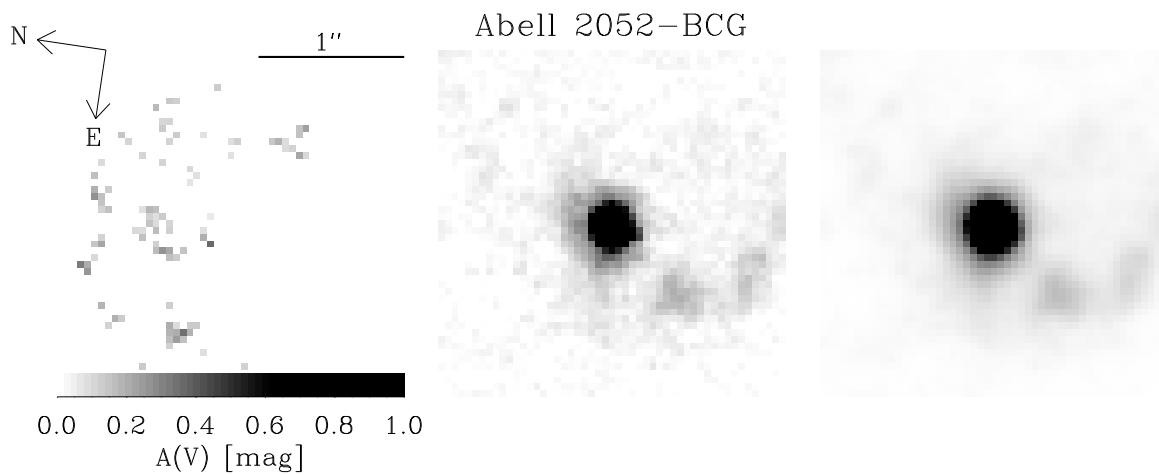


Fig. 9.— As in Figure 8, but for Abell 2052-BCG.

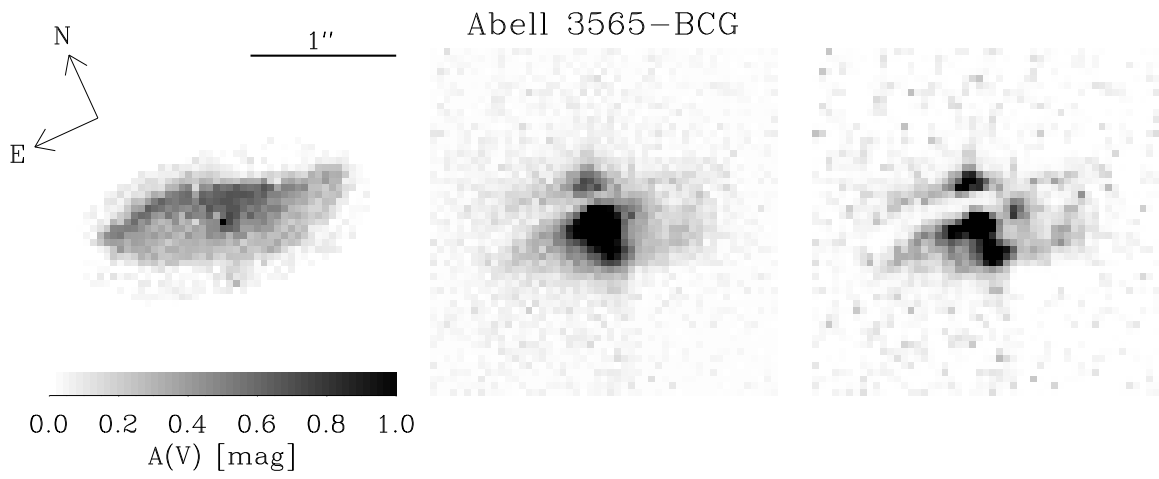


Fig. 10.— As in Figure 8, but for Abell 3565-BCG.

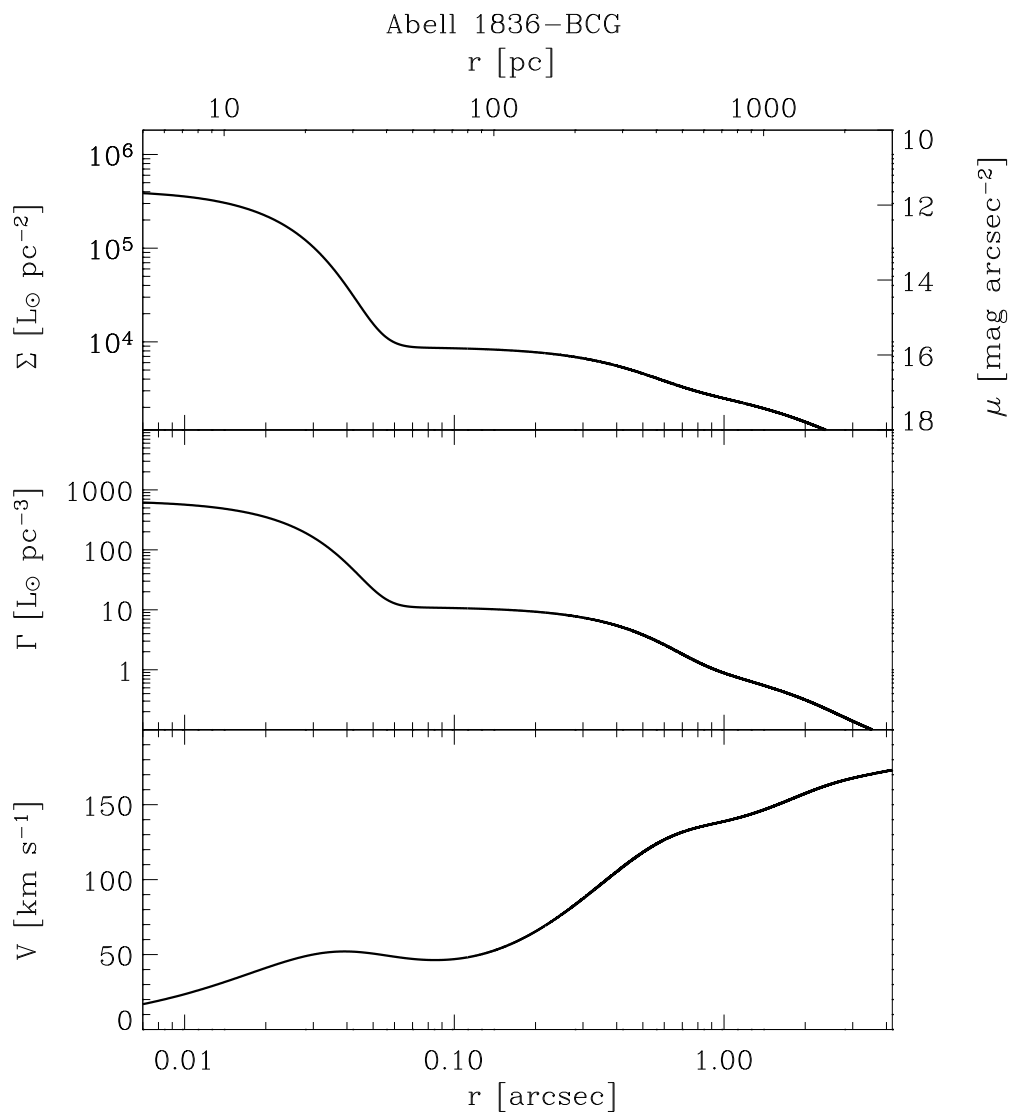


Fig. 11.— Deprojection steps for the stellar mass profile of Abell 1836-BCG. *Top panel:* Multi-Gaussian fit to the PSF-deconvolved surface brightness profile derived from the extinction-corrected WFPC2/F814W image. *Middle panel:* Deprojected stellar luminosity density profile. *Bottom panel:* Circular velocity curve assuming $(M/L)_{\star} = 1$.

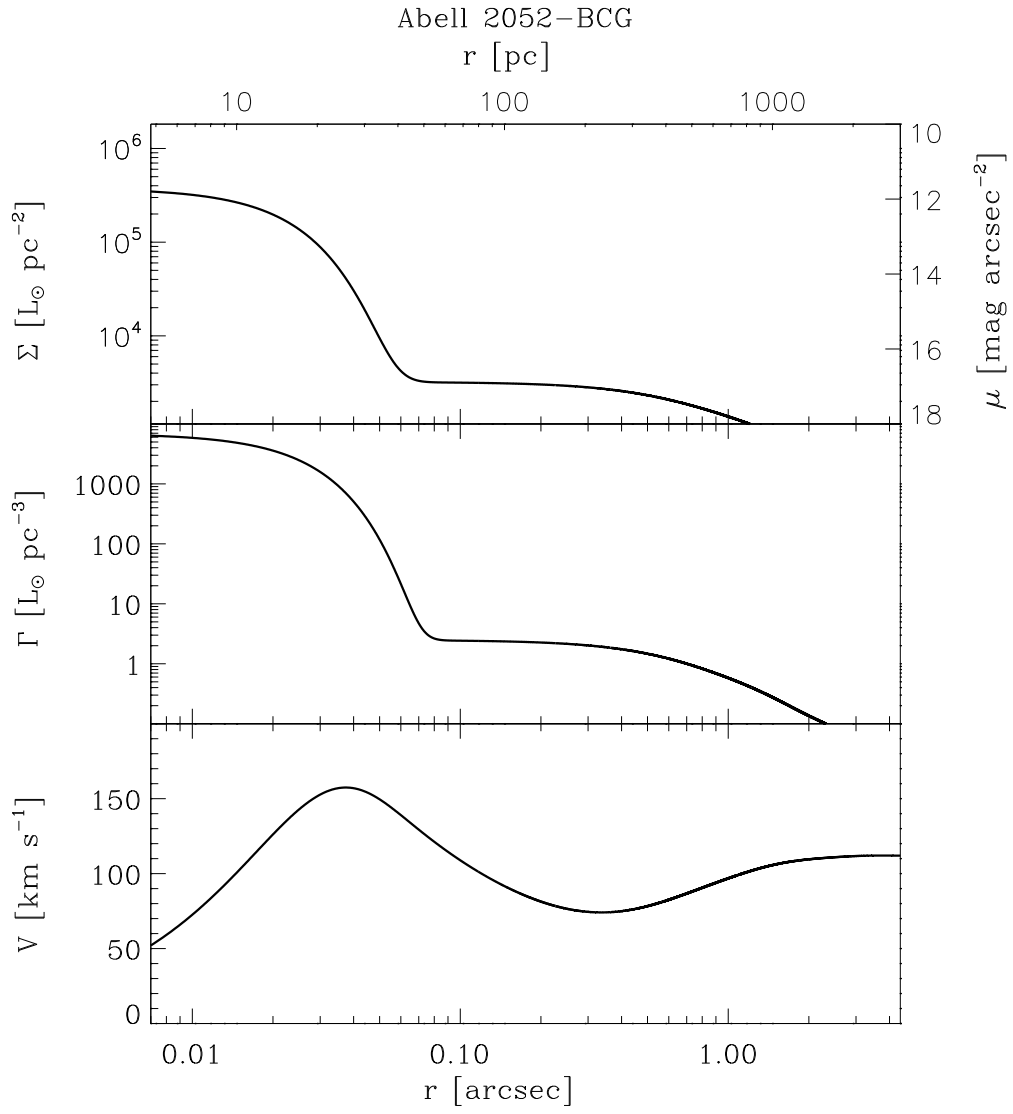


Fig. 12.— As in Figure 11, but for Abell 2052-BCG.

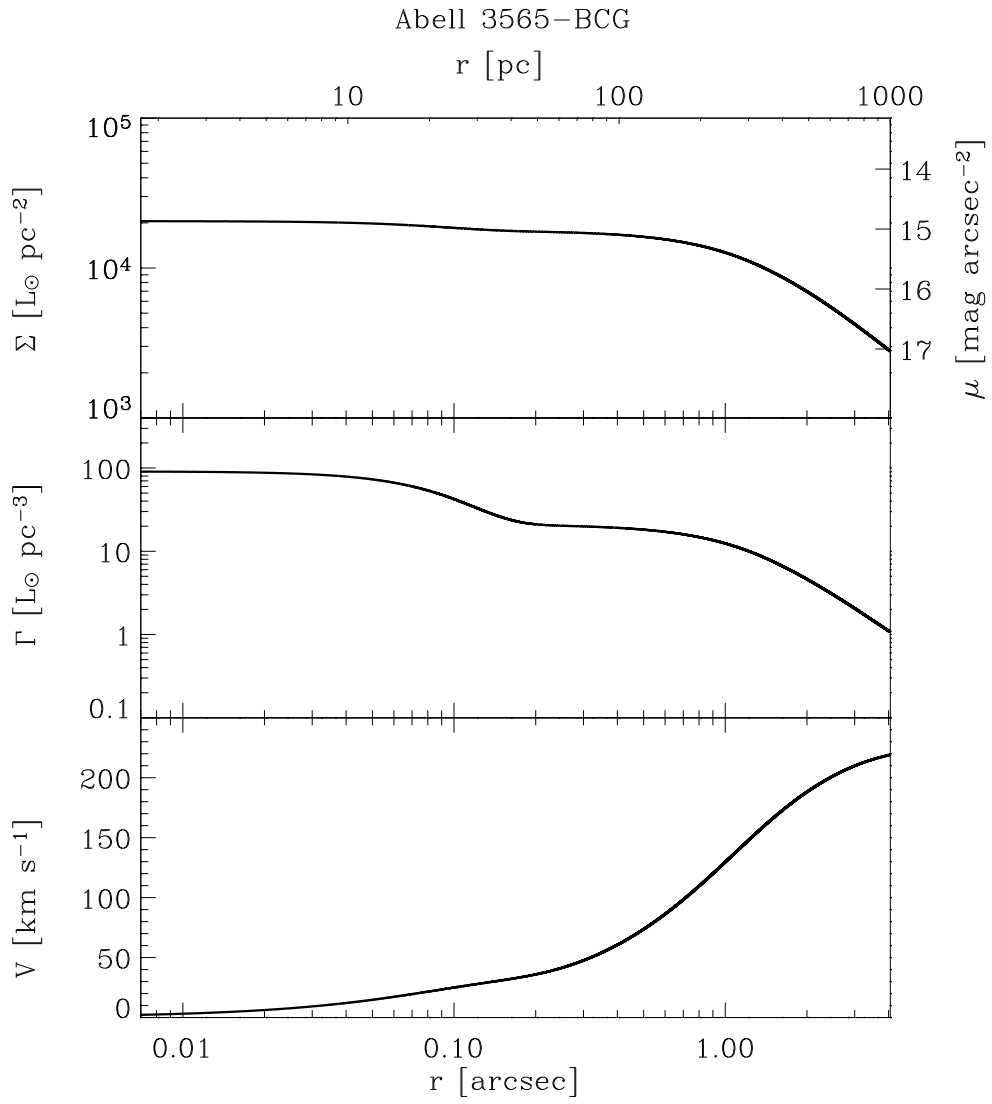


Fig. 13.— As in Figure 11, but for Abell 3565-BCG.

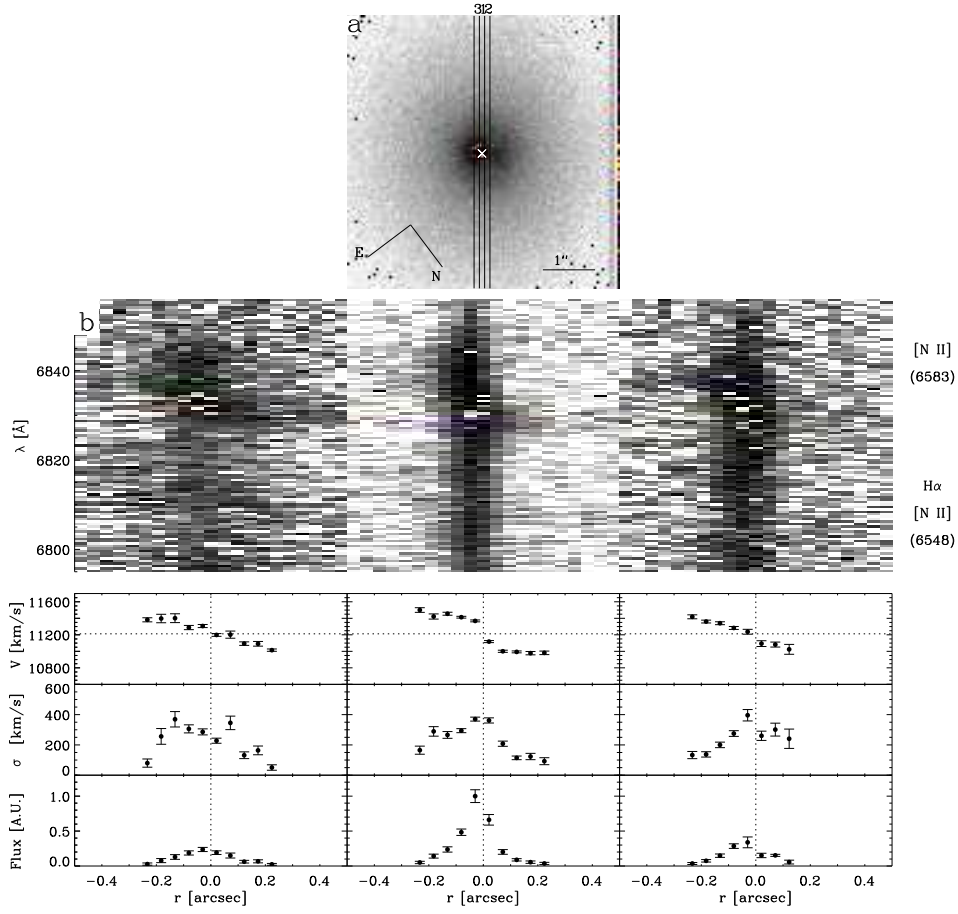


Fig. 14.— *a)* *HST* STIS/F28X50LP acquisition image of Abell 1836-BCG. The image has been rotated to the STIS instrumental frame. Orientation and scale are given. The white cross is the position of the nucleus from STIS acquisition procedure. The rectangles overplotted on the image show the actual locations of the slit during the spectroscopic observations. *b)* Portions of the bidimensional STIS spectra obtained in position 1 (major axis of the dust disk, *central panel*), 2 ($-0''.1$ offset, *left panel*) and 3 ($+0''.1$ offset, *right panel*). The spectral region centered on the $H\alpha$ emission line is shown after wavelength calibration, flux calibration and geometrical rectification. The spatial axis is horizontal and ranges between $-0''.5$ and $+0''.5$, while the wavelength axis is vertical and ranges from 6795 to 6856 Å. Individual emission lines ($[N II] \lambda 6548$, $H\alpha$, and $[N II] \lambda 6583$) are identified on the right side of the figure. *c)* $[N II] \lambda 6583$ kinematics from the spectra obtained in position 1 (*central panels*), 2 (*right panels*) and 3 (*left panels*). For each slit position the line-of-sight velocity curve (*top panel*), the radial profile of the line-of-sight velocity dispersion (uncorrected for instrumental velocity dispersion, *middle panel*), and the radial profile of line flux in arbitrary units (*bottom panel*) are given. Heliocentric velocities and velocity dispersions are not corrected for inclination and instrumental velocity dispersion, respectively.

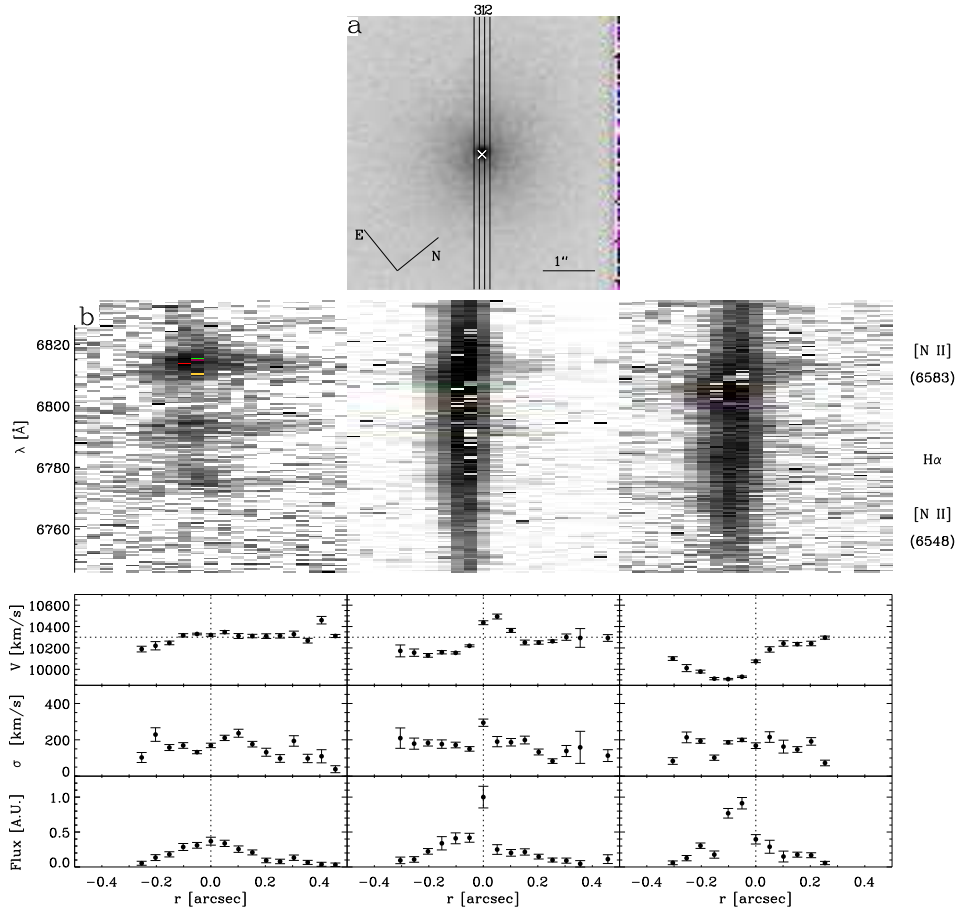


Fig. 15.— As in Figure 14, but for Abell 2052-BCG. In *b*) the spatial axis is horizontal and ranges between $-0''.5$ and $+0''.5$, while the wavelength axis ranges from 6746 to 6834 Å.

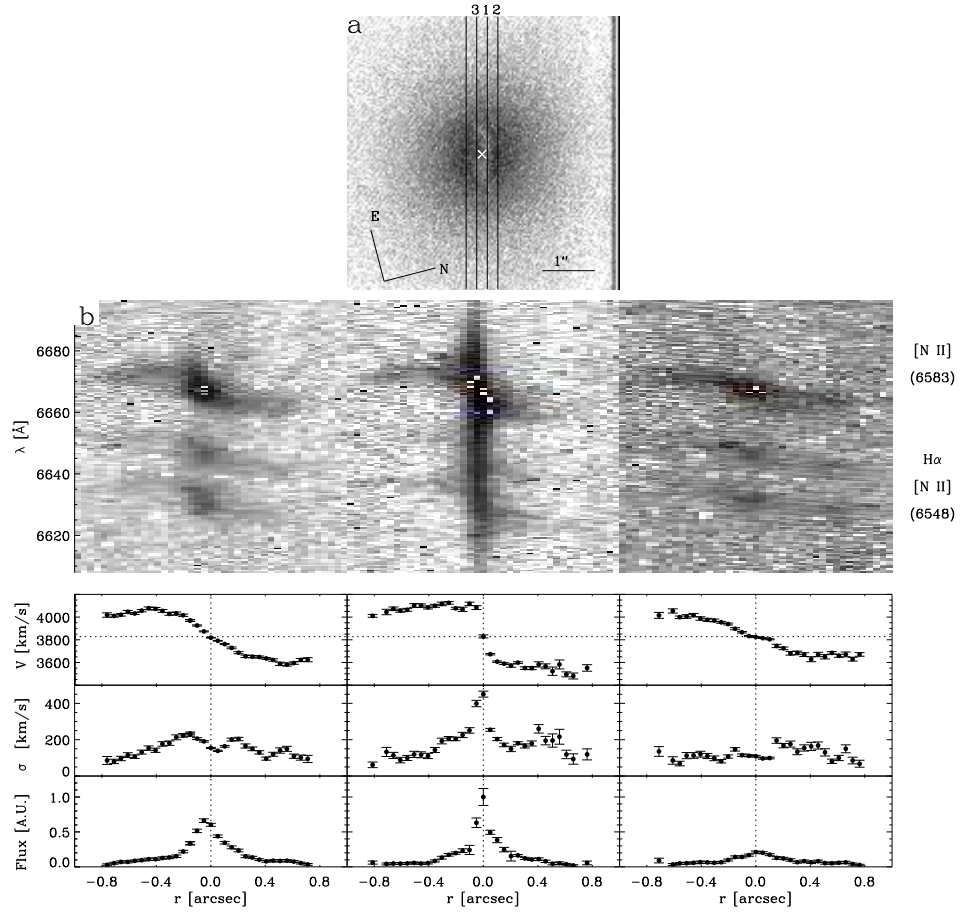


Fig. 16.— As in Figure 14, but for Abell 3565-BCG. In *b*) the spatial axis is horizontal and ranges between $-1''.0$ and $+1''.0$, while the wavelength axis ranges from 6608 to 6697 Å. Positions 2 and 3 correspond to a slit-position offset of $-0''.2$ and $+0''.2$, respectively.

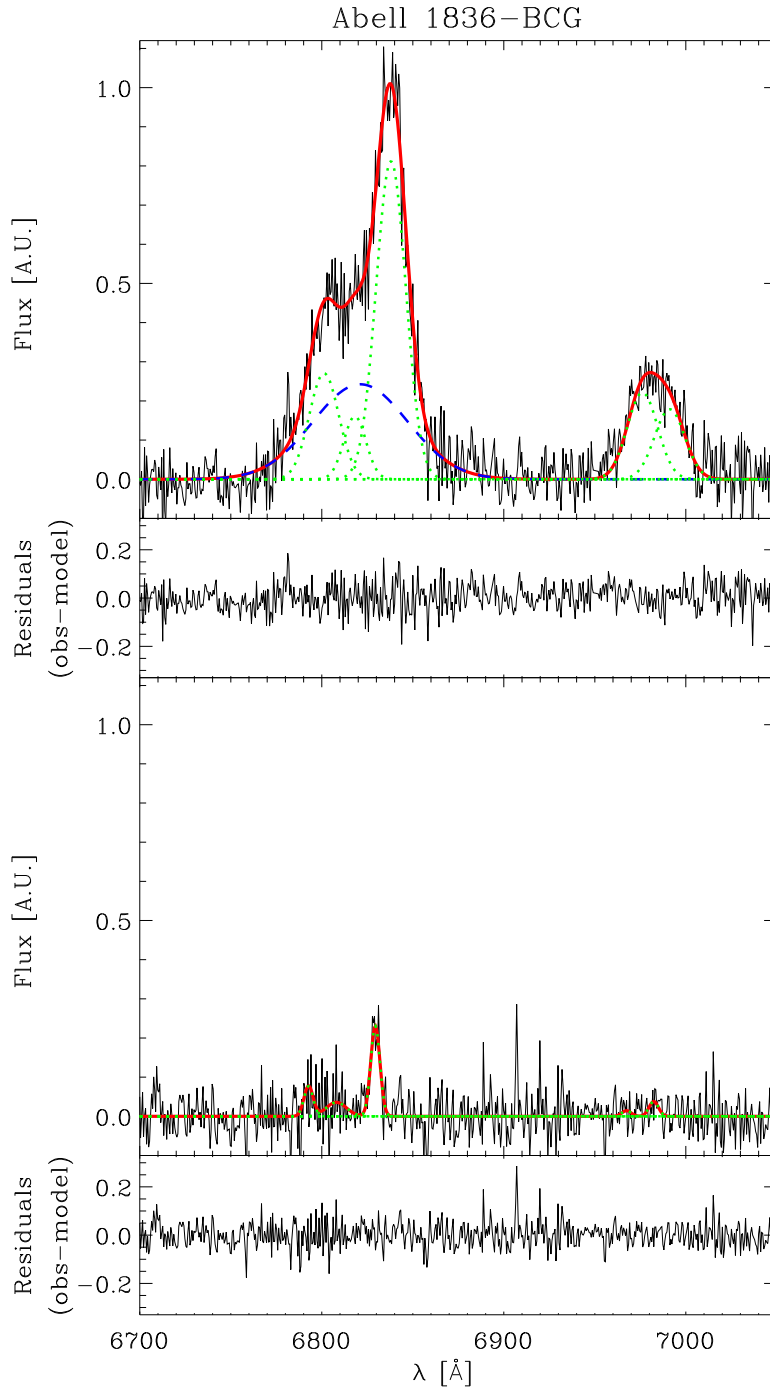


Fig. 17.— Nuclear spectrum (*upper panel*) and spectrum extracted at $r = +0''.15$ (*lower panel*), along the major axis of the dust disk of Abell 1836-BCG. Each spectrum is plotted with the Gaussian-model narrow (dotted lines) and broad (dashed lines) components, reconstructed blend, and residuals.

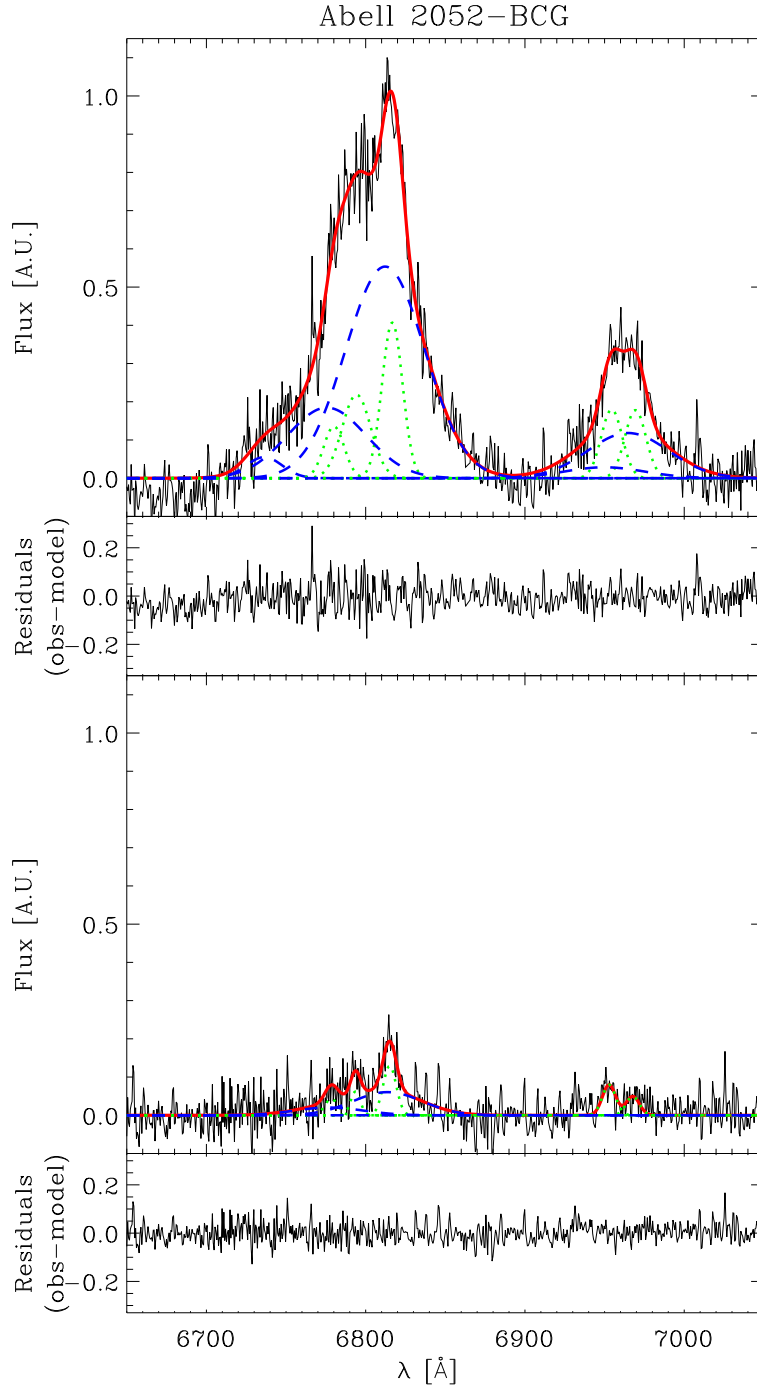


Fig. 18.— As in Figure 17, but for Abell 2052-BCG. The outer spectrum was extracted at $r = +0''.10$.

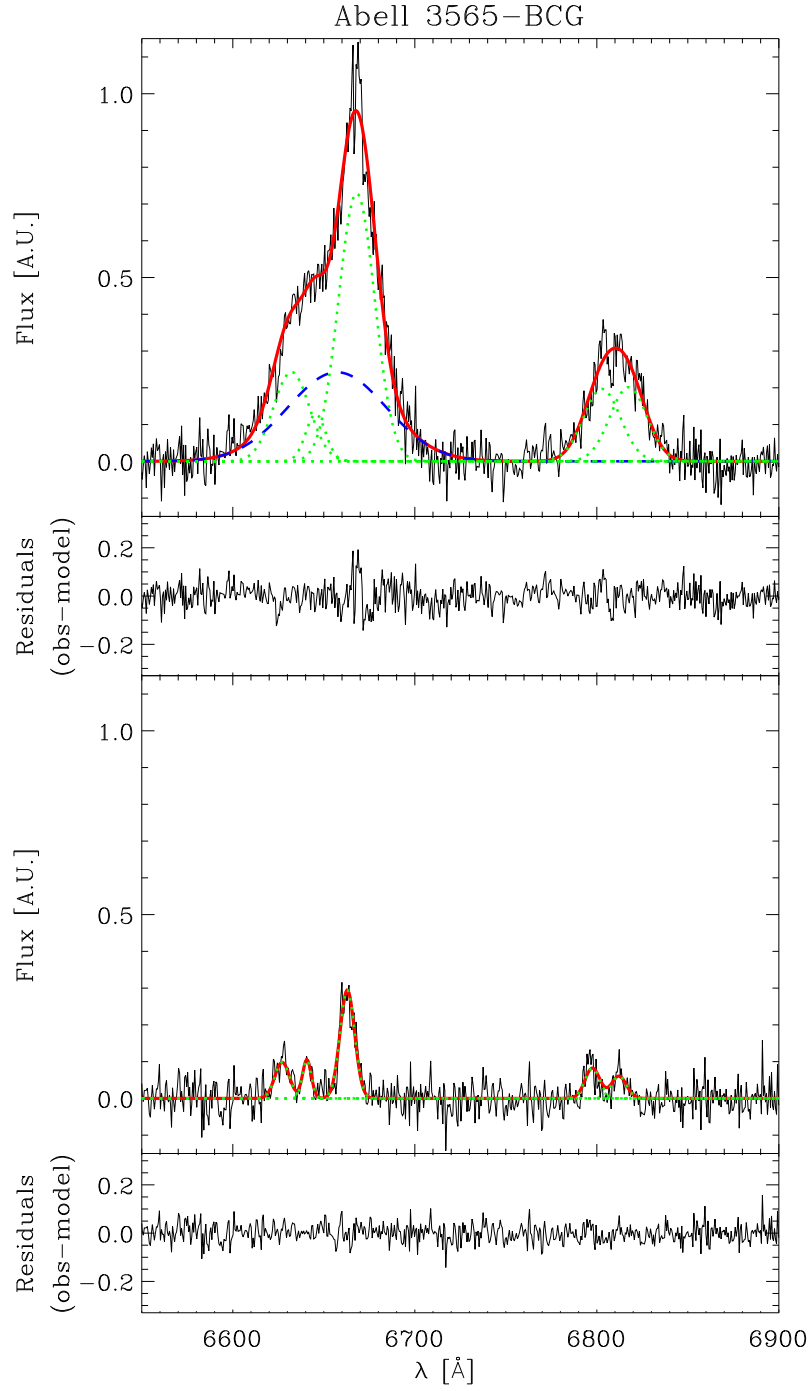


Fig. 19.— As in Figure 17, but for Abell 3565-BCG. The outer spectrum was extracted at $r = +0''.25$.

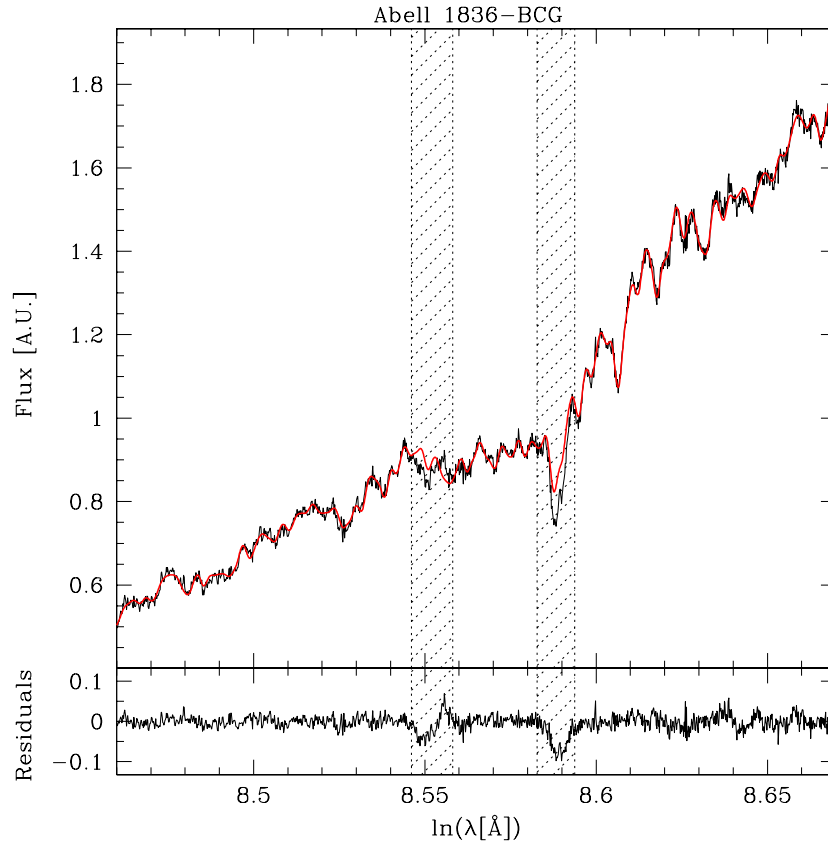


Fig. 20.— Best fit of the broadened spectrum of the template star (thick red line) to the spectrum of Abell 1836-BCG (thin black line) used to measure the galaxy velocity dispersion. The hatched regions mark the spectral ranges excluded from the fit to minimize the mismatch of the abundance ratios. The difference between the galaxy spectrum and broadened template spectrum is shown in the bottom panel.

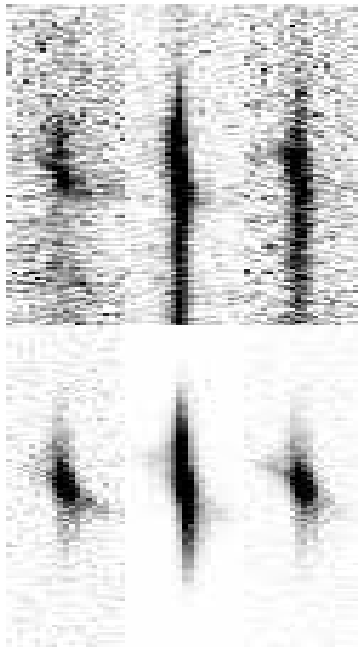


Fig. 21.— Comparison between the bidimensional observed (*upper panels*) and synthetic spectra (*lower panels*) for the best-fitting model of Abell 1836-BCG. Spectra obtained in position 1 (*central panels*), 2 (*right panels*), and 3 (*left panels*) are shown. In the models we added a random noise to mimic the actual S/N of the observed spectra.

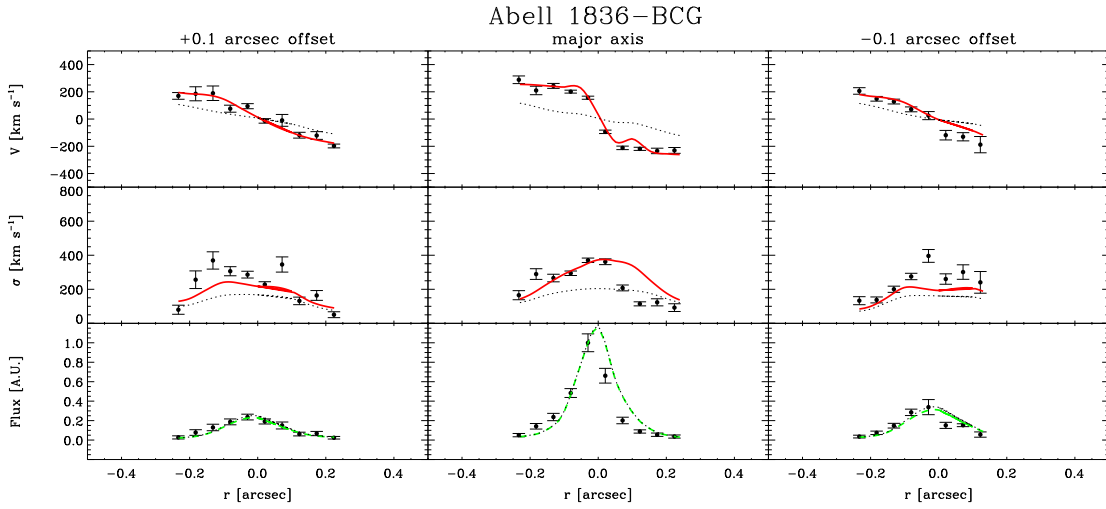


Fig. 22.— Observed [N II] $\lambda 6583$ kinematics (*filled circles*) along with the best-fitting model (*solid lines*) for the SBH mass of Abell 1836-BCG. The observed and modeled velocity curve (*top panels*), velocity dispersion radial profile (*central panels*), and flux profile (*bottom panels*) are shown for the slit along the $+0''.1$ offset position (*left panels*), the major axis (*central panels*), and the $-0''.1$ offset position (*right panels*) of the gas disk. The dotted lines correspond to a model obtained with $M_{\bullet} = 0 M_{\odot}$, $i = 69.0^{\circ}$, and $(M/L)_{\star} = 5.0 (M/L)_{\odot}$ (in the I -band).

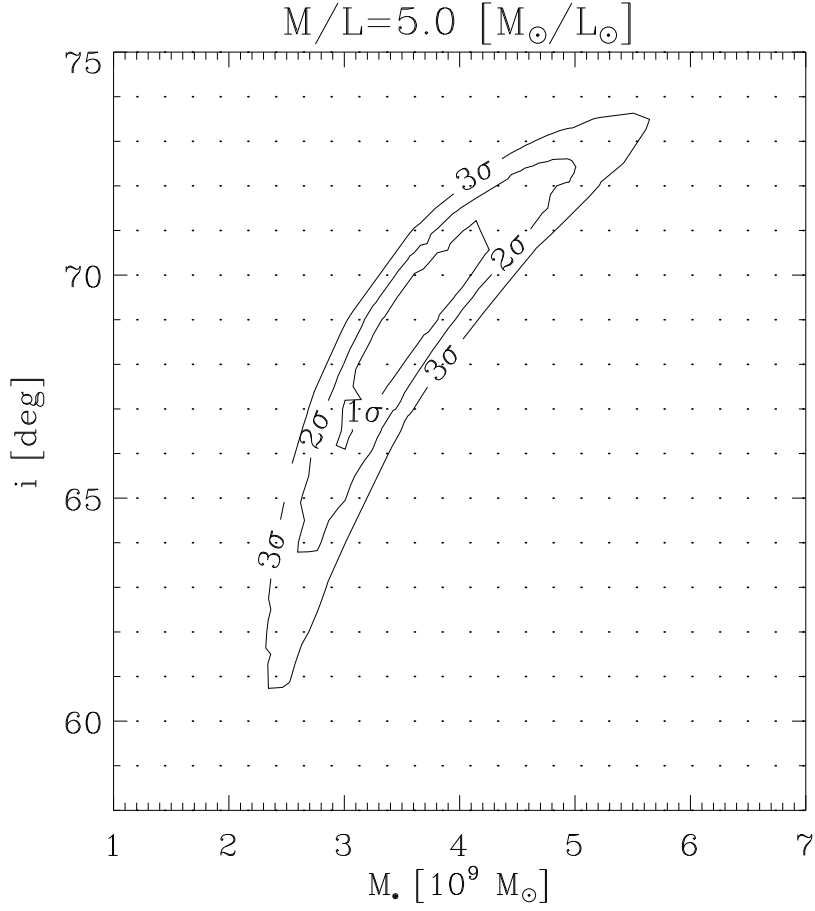


Fig. 23.— Locus of points of equal χ^2 values around the minimum χ_m^2 value for the model of Abell 1836-BCG. The 1σ , 2σ , and 3σ confidence levels expected for two free parameters are shown in the M_\bullet - i plane, with $(M/L)_\star = 5.0 (M/L)_\odot$ corresponding to the χ_m^2 value. The grid of models explored is shown by the dots.

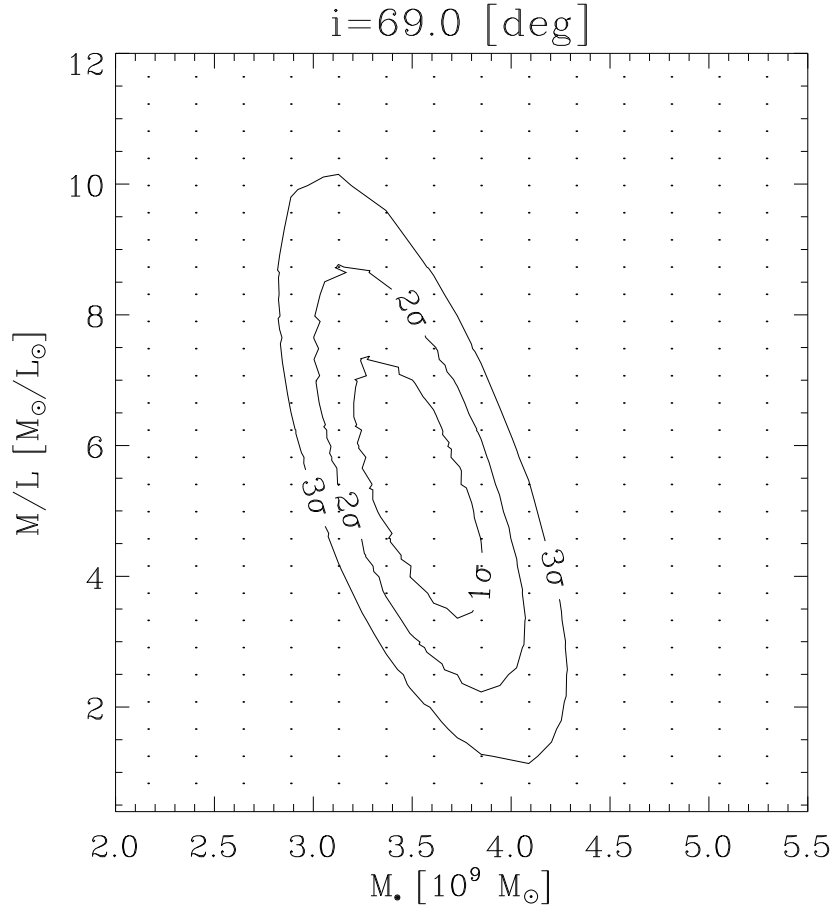


Fig. 24.— As in Figure 23, but for the 1σ , 2σ , and 3σ confidence levels expected for two free parameters shown in the M_{\bullet} - $(M/L)_{\star}$ plane with $i = 69^{\circ}$ corresponding to the χ_m^2 value.

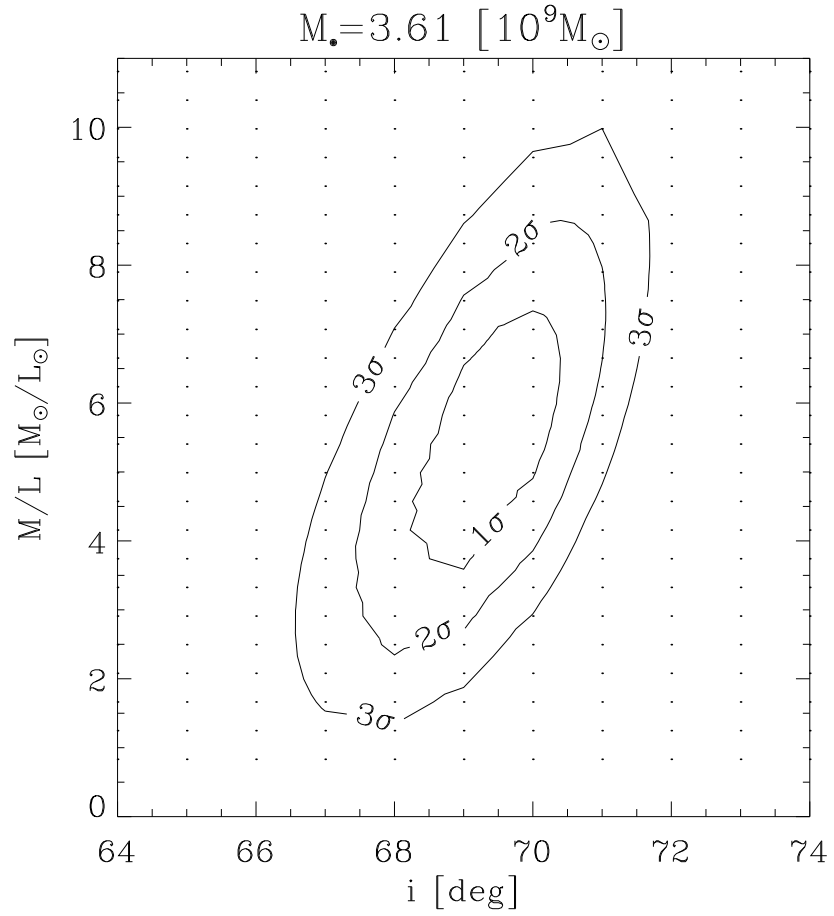


Fig. 25.— As in Figure 23, but for the 1σ , 2σ , and 3σ confidence levels expected for two free parameters shown in the i – $(M/L)_{\star}$ plane with $M_{\bullet} = 3.61 \cdot 10^9 M_{\odot}$ corresponding to the χ_m^2 value.

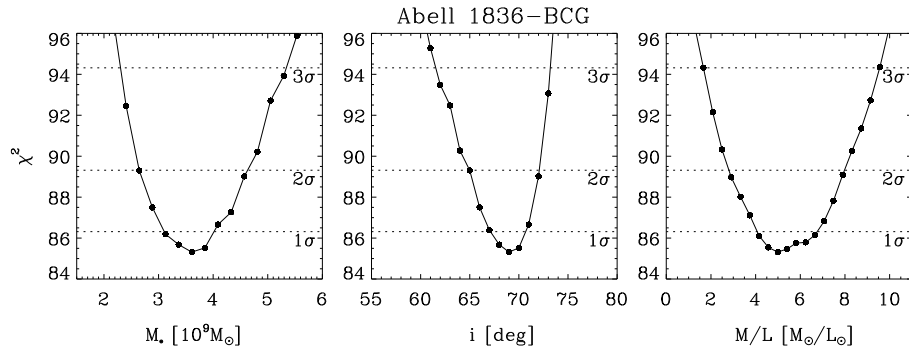


Fig. 26.— χ^2 distribution for Abell 1836-BCG as a function of M_\bullet (*left*), inclination (*center*), and $(M/L)_\star$ (*right*). The dotted horizontal lines indicate the confidence levels on the best fitting values, marginalizing over all other parameters.

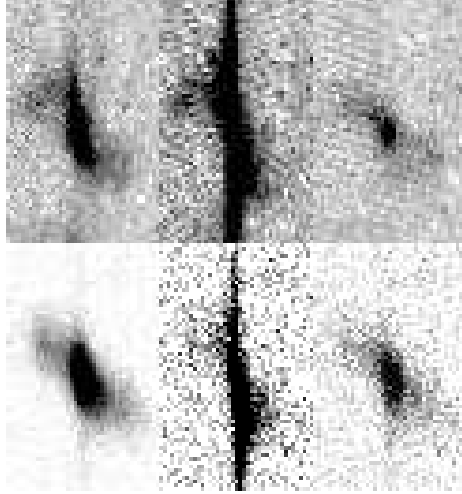


Fig. 27.— As in Figure 21, but for Abell 3565-BCG.

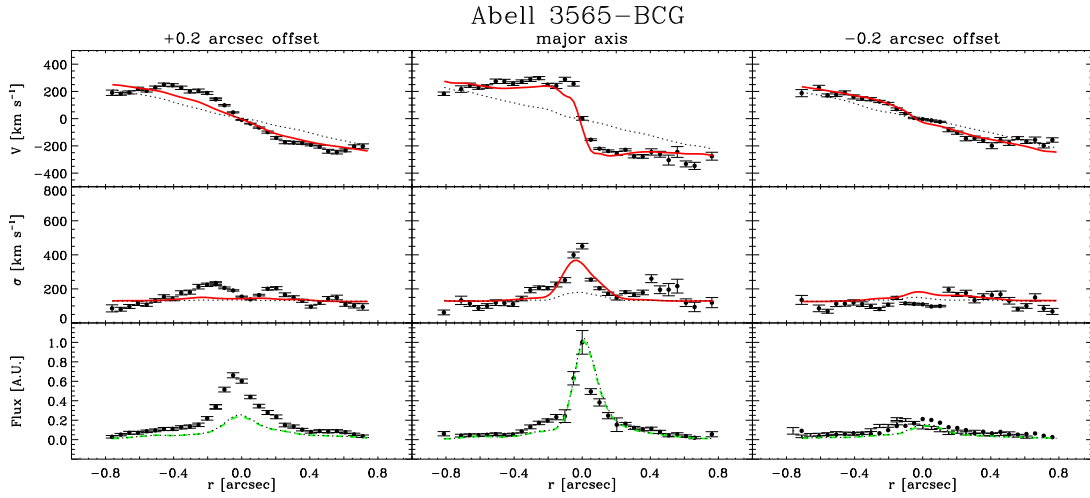


Fig. 28.— Observed [N II] $\lambda 6583$ kinematics (*filled circles*) along with the best-fitting model (*solid lines*) for the SBH mass of Abell 3565-BCG. The observed and modeled velocity curve (*top panels*), velocity dispersion radial profile (*central panels*), and flux profile (*bottom panels*) are shown for the slit along the $+0''.1$ offset position (*left panels*), the major axis (*central panels*), and the $-0''.1$ offset position (*right panels*) of the gas disk. The dotted lines correspond to a model obtained with $M_{\bullet} = 0 M_{\odot}$, $i = 66.0^{\circ}$, and $(M/L)_{\star} = 6.3 (M/L)_{\odot}$ (in the I -band).

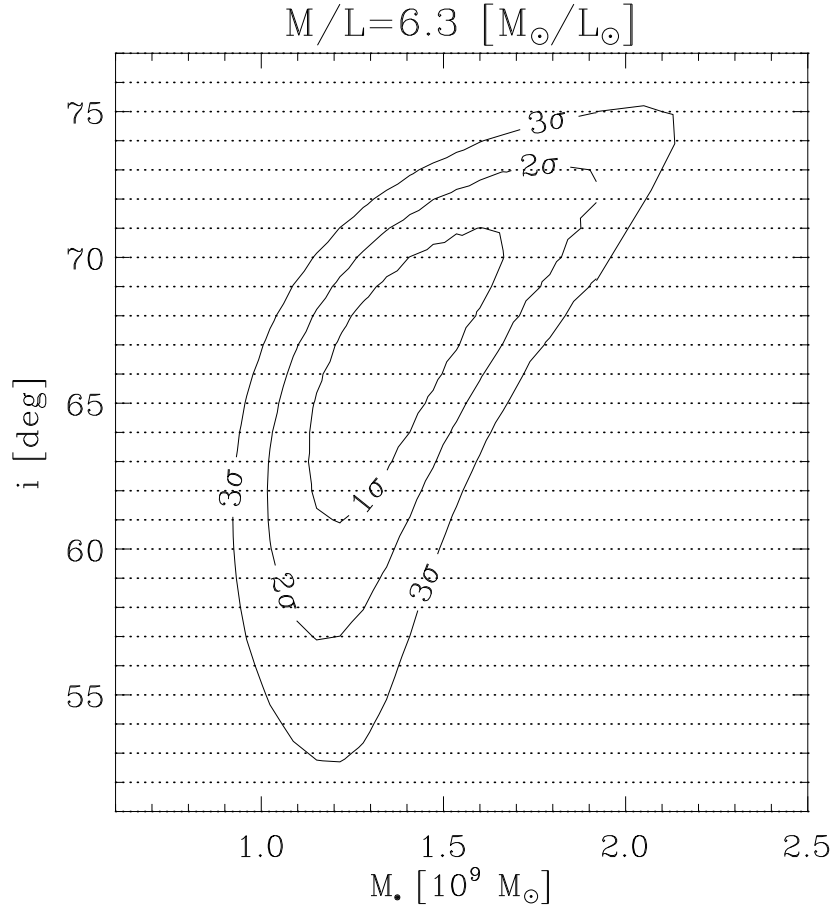


Fig. 29.— Locus of points of equal χ^2 values around the minimum χ_m^2 value for the modeling of Abell 3565-BCG. The 1σ , 2σ , and 3σ confidence levels expected for two free parameters are shown in the M_{\bullet} - i plane, with $(M/L)_{\star} = 6.3 (M/L)_{\odot}$ corresponding to the χ_m^2 value.

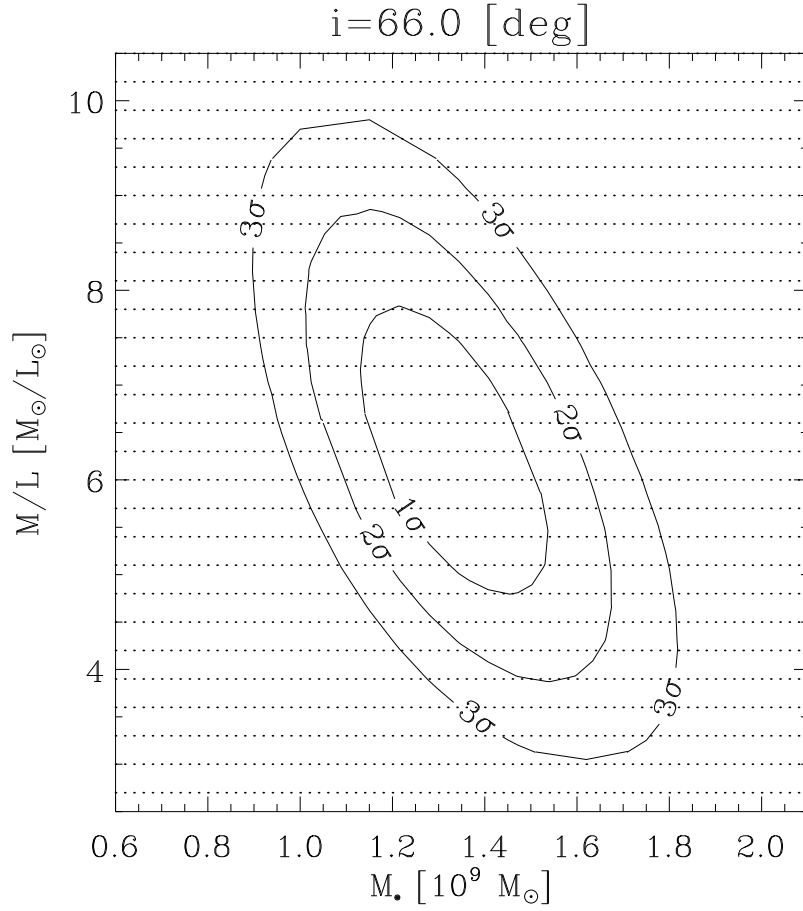


Fig. 30.— As in Figure 29, but for the 1σ , 2σ , and 3σ confidence levels expected for two free parameters shown in the $M_{\bullet}-(M/L)_{\star}$ plane with $i = 66^{\circ}$ corresponding to the χ_m^2 value.

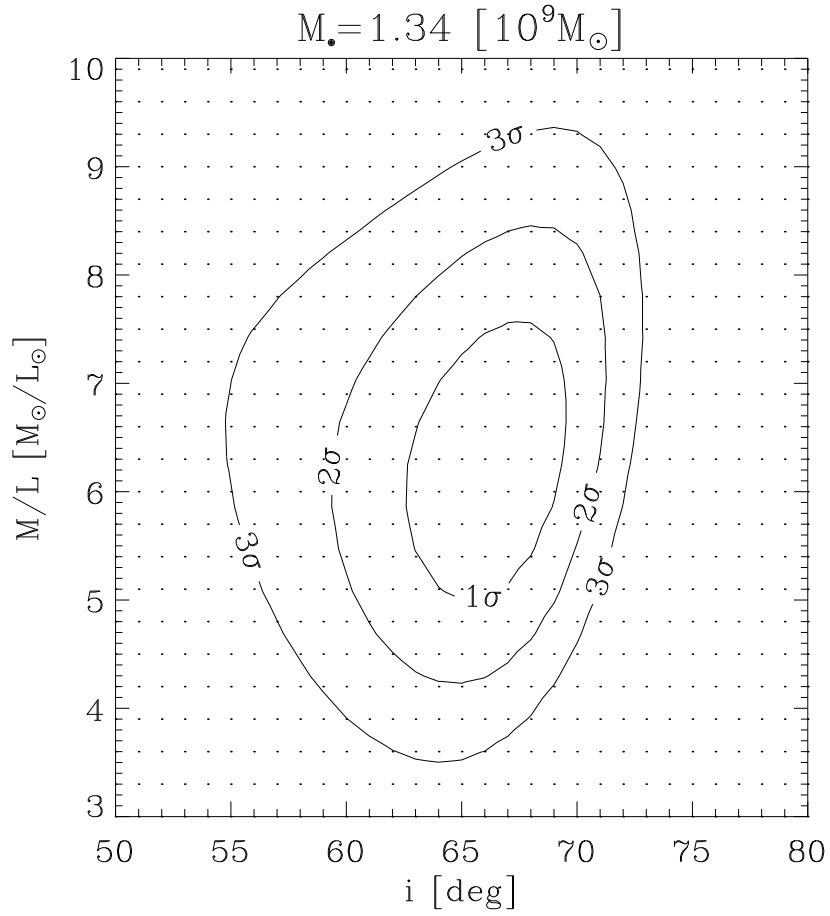


Fig. 31.— As in Figure 29, but for the 1σ , 2σ , and 3σ confidence levels expected for two free parameters shown in the i – $(M/L)_*$ plane with $M_\bullet = 1.34 \cdot 10^9 M_\odot$ corresponding to the χ_m^2 value.

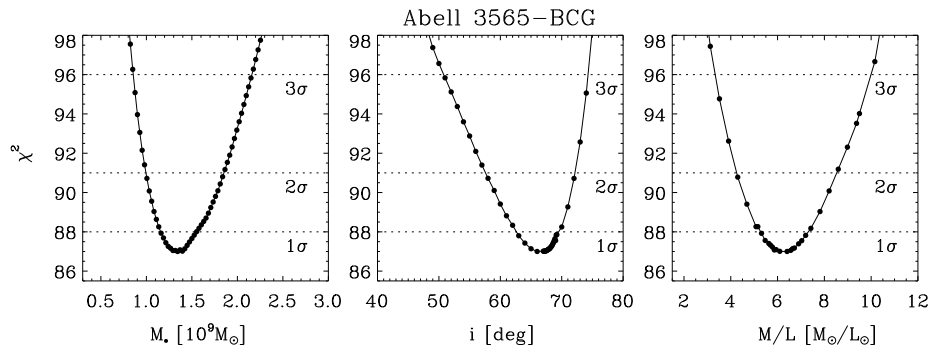


Fig. 32.— Same of Figure 26, but for Abell 3565-BCG.

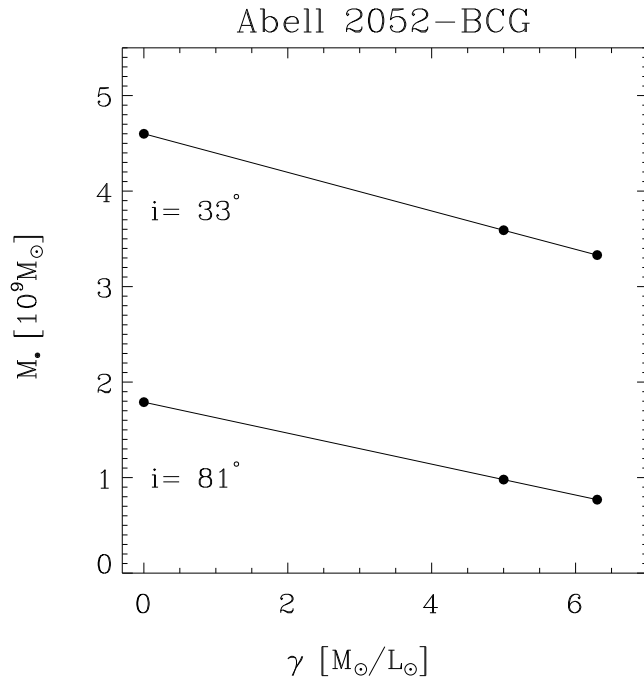


Fig. 33.— Upper limit of SBH mass of Abell 2052-BCG as function of the $(M/L)_{\star}$ assumed, for an inclination of the gas-disk $i = 33^{\circ}$ and $i = 81^{\circ}$.

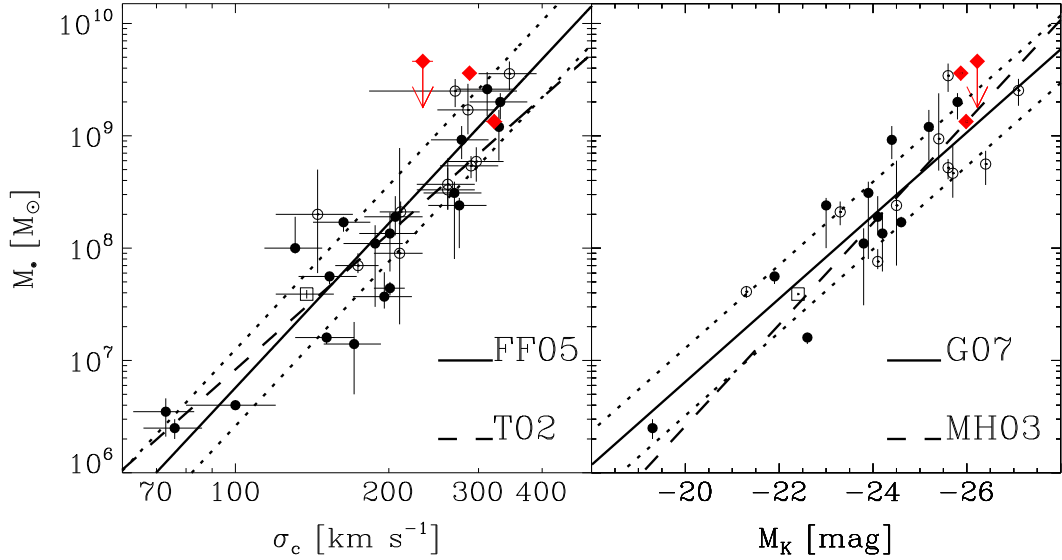


Fig. 34.— *Left panel:* Location of the SBHs masses of our BCG sample galaxies (*diamonds*) with respect to the M_{\bullet} – σ_c relation by Ferrarese & Ford (2005). We plot the SBH masses based on resolved dynamical studies of ionized gas (*open circles*), water masers (*open squares*), and stars (*filled circles*) from Table 2 of Ferrarese & Ford (2005). The dashed line represents the Tremaine et al. (2002) relation. *Right panel:* Location of our BCG sample galaxies with respect to the near-infrared (K -band) M_{\bullet} – L_{bulge} relation by Graham (2007). Data are taken from Table 2 of Graham (2007) and symbols are as in the left panel. Masses and magnitudes of NGC 5252, NGC 6251 and Cygnus A were adjusted to a distance obtained with $H_0 = 75 \text{ km s}^{-1} \text{ Mpc}^{-1}$. The dashed line represents the Marconi & Hunt (2003) relation. In both panels, we added the data relative to NGC 1399 (Houghton et al. 2006) and the dotted lines represent the 1σ scatter in M_{\bullet} .